Numerical Analysis of Optically-induced Long-period Fiber Gratings for Sensing Applications

Chaofan Wang

Thesis submitted to the faculty of the Virginia Polytechnic Institute and State University in partial fulfillment of the requirements for the degree of

Master of Science
In
Electrical Engineering

Anbo Wang, Chair
Gary R. Pickrell
Yizheng Zhu

August 27, 2014
Blacksburg, VA

Keywords: OLPG, traveling LPG, distributed sensing, few mode fiber, mode conversion

Numerical Analysis of Optically-induced Long-period Fiber Gratings for Sensing Applications

Chaofan Wang

ABSTRACT

Long-period fiber gratings (LPGs) with a period ranging from several hundred micrometers to a few millimeters can couple a core mode to discrete co-propagating cladding modes when the phase matching condition is satisfied. The rapid attenuation of cladding modes results in loss bands in the transmission spectrum. As the attenuation bands are sensitive to the LPG period and the fiber surrounding environment such as temperature, strain and ambient refractive index, LPGs can be used for sensing. However, traditional LPGs with gratings inscribed in the fibers can only sense a single point and cannot be used for distributed sensing. Although new ideas were proposed to use traveling LPG formed by a pulsed acoustic wave, the large attenuation of the acoustic wave in the fiber greatly limits the sensing range to only several meters.

In this thesis, we proposed to use a traveling LPG formed by the interference of two high power co-propagating core modes, usually LP_{01} and LP_{11}. The beating of the two modes will induce a refractive index grating due to the optical Kerr effect, and the grating is called optically induced long-period fiber grating (OLPG). Compared to the grating induced by acoustic waves, OLPG is able to travel for a long distance due to the small attenuation of the guided core modes. Mode conversion in the OLPG is numerically simulated and analyzed using the finite-difference beam propagation method (FD-BPM). The result shows full conversion for both core-core and core-cladding mode coupling under phase matching condition. Moreover, the sensitivity of OLPG to temperature, axial strain and ambient refractive index is investigated and analyzed. It is seen that the sensitivities of temperature and axial strain with OLPG are different from the traditional LPGs since the period variation in OLPG is caused by the effective index difference of the two core modes at the writing wavelength, while in the traditional LPGs it is directly induced by temperature or strain. For the refractive index sensitivity with a large

cladding, OLPG behaves the same as a traditional LPG with only material contributions since the grating period remains unchanged.

Acknowledgements

I would like to express my deepest gratitude to my advisor, Dr. Anbo Wang, for providing me with an excellent atmosphere for doing research. Without his excellent guidance the research would not move on.

I would like to thank Lingmei Ma for her excellent guidance and helpful discussion on my research.

I would also like to thank other CPT members, Nan Wu, Zhipeng Tian, Bo Liu and Chennan Hu for their help, encouragement, and friendship over the past two years. I have had a wonderful time with all the CPT members.

Finally, I would like to thank my parents for their endless supports during my whole life.

Table of Contents

List of Figures

Chapter 1
Introduction

Long-period fiber gratings (LPGs) are formed by periodic variation of refractive index [1] whose periods are generally in the range from several hundred micrometers to a few millimeters. The long period makes it possible to have mode conversion between two co-propagating modes (usually from LP_{01} to a cladding mode) whose beating length, according to the mode coupling theory, is equal to the period. The attenuation of cladding modes results in the attenuation bands centered at discrete wavelengths in the transmission spectrum, with each wavelength corresponding to the coupling to a different cladding mode. Since the centers of attenuation bands are sensitive to the LPG period and local environment like temperature, strain, bending and refractive index of ambient medium, LPGs can be used for sensing, with many work [2-6] demonstrated over the past 20 years. However, for a fixed LPG inscribed in the fiber, the sensing is limited only at a local point, making it impossible to have distributed sensing. Although we can fabricate many LPGs along the whole fiber, the work is tedious and impossible for large amount of sensing points. An alternative method is to use traveling LPGs, but the difficulty comes from how to generate such LPGs. It has been demonstrated that a traveling LPG can be formed by a pulsed acoustic wave [7] traveling through the fiber. However, the acoustic wave can only propagate to several meters which is not applicable for long-range sensing. In this thesis, we proposed a traveling LPG induced by the optical Kerr effect for distributed fiber sensing. The principle is to let two high power modes, usually LP_{01} and LP_{11}, travel through a few mode fiber. During the propagation, the beating of the two modes will result in a refractive index variation (gratings) due to the Kerr effect. Moreover, the small attenuation of the core modes will ensure that the OLPG can travel for a long distance which greatly increases the sensing range.

This thesis focuses on providing a comprehensive numerical simulation and analysis of OLPG-based distributed fiber sensors.

1.1 Motivation

Distributed fiber sensing has been attractive for many years. Three main principles have been demonstrated: Rayleigh scattering [8], Raman scattering [9] and Brillouin scattering [10]. Among these three mechanisms Brillouin scattering method has been developed widely in recently years due to its response to both temperature and strain [11, 12]. Raman scattering is limited only to temperature sensing since the intensity of Raman scattered light is independent of strain. Rayleigh scattering has some applications in sensing attenuation, phase interference, polarization [13, 14] and can be also used for temperature and strain measurement using Optical Frequency Domain Reflectometry (OFDR) [15].

Of all the distributed sensing mechanisms, there is no mature technique for fully distributed sensing of ambient medium like refractive index. Since it is known that LPGs can be used to measure the refractive index of the ambient medium, it is natural to assume using traveling LPGs for distributed fiber sensing.
OLPG [16] is a great tool to satisfy both distributed sensing and ambient index sensing. Furthermore, it can be also used to measure other local environment like temperature, strain and bending.

1.2 Outline

The thesis is structured as follows: In Chapter 2, traditional LPG is introduced including the fabrication, theory and its application as a sensor. Chapter 3 illustrates the principle of OLPG and its sensing applications. A numerical tool - finite-difference beam propagation method (FD-BPM) is introduced to simulate the mode conversion in OLPG and further to analyze the sensitivity of OLPG to temperature, axial strain and refractive index. Moreover, a detailed sensing system is also introduced and analyzed. Chapter 4 presents the summary of the work and some suggestions for future work.

Chapter 2

Characteristics and sensing applications of Long-period gratings

In this chapter, we will present a review of traditional LPGs including the LPG fabrication (Section 2.1), LPG theory (Section 2.2), and some general LPG sensors (Section 2.3).
The theory and characteristics of OLPG will be introduced in Chapter 3.

2.1 Fabrication of long-period gratings

The inscription of an LPG is to achieve periodic perturbation of refractive index either in the core, or cladding or both. Compared to an FBG, an LPG has a longer period from several hundred micrometers to a few millimeters and similar index modulation from 10^{-4} to 10^{-5}. Vengsarkar firstly proposed the inscription of LPG using UV (242-248 nm) exposure directly on the core of a hydrogen loaded Ge-doped fiber [17]. Over the past two decades, UV radiation is still the most commonly used and well established method. Meanwhile, other techniques are also used such as the residual thermal stress [18], the photoelasticity and the geometrical modulation of the cladding structure [15, 19].

2.1.1 UV radiation

The UV radiation technique has been successfully used for making FBGs [20, 21], and it also applies to LPGs. Two common techniques are used to inscribe an LPG in Ge-doped fibers: the point to point technique and the amplitude mask [17]. The desired index modulation is related to the selected UV light (193-360 nm), the exposure time and the power of the inscribed laser. In Figure 2-1(a), the point to point method is illustrated with a focused UV beam exposed to the core of the fiber through a thin slit aperture. A period of Λ is formed by moving the fiber a distance of Λ in the longitudinal direction. For the amplitude mask technique, the optical fiber is scanned by the UV light through a amplitude mask which contains an array of transparent windows to form a periodic refractive index pattern, as illustrated in Figure 2-1(b). Both techniques are simple and

flexible. The amplitude mask technique is more appropriate for mass production while the point to point technique is cheaper and more flexible.

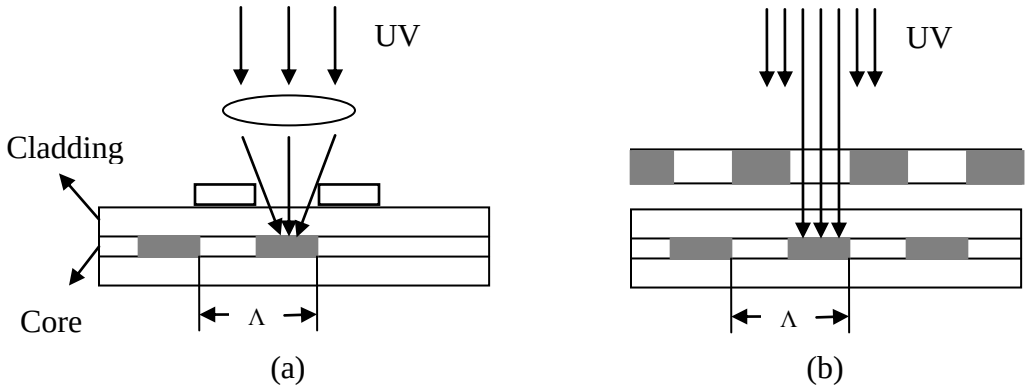

Figure 2-1 UV inscription techniques: (a) point to point and (b) amplitude mask.

UV exposure will induce a Gaussian like profile with azimuthal symmetry. Thus, according to the mode coupling theory, it supports the conversion between HE_{11} core mode and HE_{1m} or EH_{1m} cladding mode. UV exposure also induces birefringence which can produce a polarization splitting in the attenuation bands for LPGs inscribed in non polarization-maintaining fibers [22]. The disadvantages of UV radiation technique are the temperature limitation <250 ℃ and high fabrication equipment cost [23].

2.1.2 LPG inscription by residual thermal stress

The heating and sudden cool down of the glass of a fiber will change the viscosity and therefore the index of refraction, either in the fiber core or cladding. General methods include the radiation by CO_2 [24] or femtosecond lasers [25] and electric arc [26]. One difference from the UV radiation is the non-uniform refractive index profile in the transverse plane, allowing the conversion between LP_{01} to asymmetric cladding modes. In Figure 2-2(a), a fiber is radiated by a CO_2 laser using the point to point technique. Since silica is not transparent at 10 μm, it will absorb the energy of CO_2 laser. Then the fiber will undergo heating and cool down processes to induce the change of refractive index. Normally it is required to have 10W power in a continuous wave CO_2 laser. Compared to the UV radiation technique, CO_2 laser has been shown to produce LPGs with high temperature and polarization insensitivity [24], and with the spectrum stable

even after annealing at 1200 ℃ [27]. In the electric arc method, optical fibers are heated by electric arc discharge generated usually by a fusion splicing machine, as shown in Figure 2-2(b). The mechanisms include the induction of microbends into the fiber [19], the diffusion of dopants [28, 29], the periodic tapering of fiber [30] and the internal stress relaxation [26]. Such LPGs are shown to be operated at temperatures up to 800 ℃ [31], and 1190 ℃ [26] if annealed appropriately. Usually the exposure region by an electric arc is the order of 100 μm which limits the minimum LPG period.

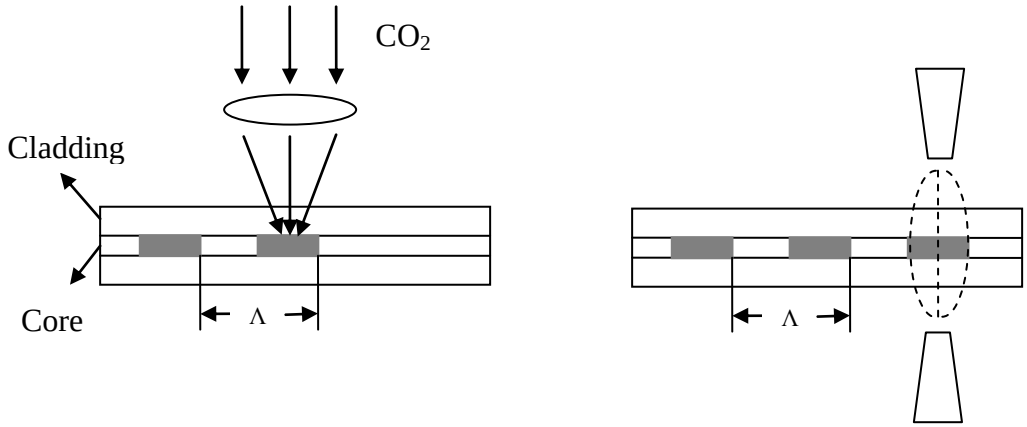

Figure 2-2 LPG inscription by (a) CO_2 radiation and (b) electric arc techniques.

2.1.3 LPG inscription by mechanical stress

Due to the photoelastic effect [32], the index of refraction can be modulated when imposing a stress on a glass. Therefore LPGs can be induced through mechanical stress. Figure 2-3 illustrates a typical example of periodic microbending and pressure points. The advantages of this technique are its simplicity, flexibility and low cost. This technique is usually used in a corrugated design.

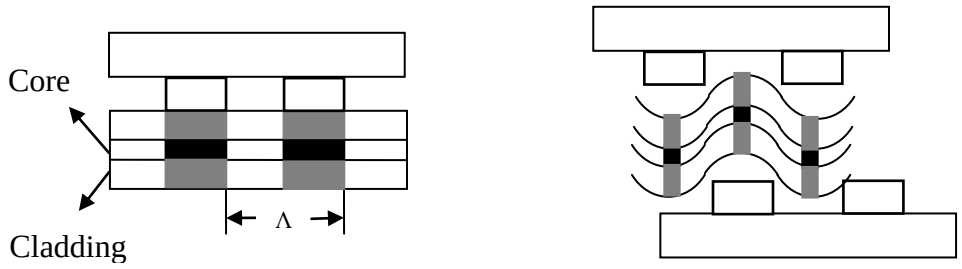

(a) (b)

Figure 2-3 LPG induced by stress through (a) pressure points and (b) microbending

2.1.4 LPG inscription by etching

Chemical etching of the cladding to form a corrugated structure has been shown to generate an LPG [33]. Usually we place a photomask over the fiber, and then immerse the fiber in a hydrofluoric acid solution to generate a periodic grating. The diameter in the etched regions is controlled by the exposure time and the concentration of the solution. Disadvantages of this method are their low repeatability and difficulty to control the corrugated structure.

2.2 Coupled mode theory

Mode coupling theory is used to explain the behavior of mode conversion when a propagating mode is traveling through an area with small refractive index perturbation. Detailed introduction and derivation is illustrated in [34]. In the case of LPG, we consider the coupling between forward propagating modes, the coupled mode equations are simply written as [23]:

$$\frac{dA_{co}(z)}{dz} = i\sum_{m} B_m(z)C_{co-m}(z), \tag{2.1}$$

$$\frac{dB_j(z)}{dz} = iA_{co}(z)C_{j-co} + i\sum_{m\neq j} B_m(z)C_{j-m}(z). \tag{2.2}$$

Assuming a small and uniform refractive index perturbation $\Delta n(r,z)$, the coupling coefficient is:

$$C_{co-m} = \frac{k}{2\eta_0}\int_A n(r)\Delta n(r,z)\vec{E}_{co}^{*}(\vec{r})\vec{E}_m(\vec{r})e^{-i(\beta_{co}-\beta_m)z}dA, \tag{2.3}$$

where $C_{m-co} = (C_{co-m})^*$, $\vec{E}_{co}, \vec{E}_m$ are the normalized electric fields for initial core mode and converted cladding modes, respectively. A is the whole integration transverse area.

Consider a sinusoidal refractive index modulation

$$\Delta n(r,z) = \begin{cases} \Delta n_{co}\cos(\dfrac{2\pi}{\Lambda}z + \phi_{co}),\ r \le a_1 \\ \Delta n_{cl}\cos(\dfrac{2\pi}{\Lambda}z + \phi_{cl}),\ a_1 \le r \le a_2 \\ 0,\ r > a_2 \end{cases}. \tag{2.4}$$

The coupling coefficient can be written as:

$$\begin{aligned} C_{co-m} &= \frac{k}{2\eta_0}\int_A n(r)\Delta n(r,z)\vec{E}_{co}^{*}(\vec{r})\vec{E}_m(\vec{r})e^{-i(\beta_{co}-\beta_m)z}dA, \\ &= \frac{k}{4\eta_0}n_{co}\Delta n_{co}\left[e^{i\phi_{co}}e^{i(\frac{2\pi}{\Lambda}-(\beta_{co}-\beta_m))z} + e^{-i\phi_{co}}e^{-i(\frac{2\pi}{\Lambda}+(\beta_{co}-\beta_m))z}\right]I_{1m} \\ &\quad + \frac{k}{4\eta_0}n_{cl}\Delta n_{cl}\left[e^{i\phi_{cl}}e^{i(\frac{2\pi}{\Lambda}-(\beta_{co}-\beta_m))z} + e^{-i\phi_{cl}}e^{-i(\frac{2\pi}{\Lambda}+(\beta_{co}-\beta_m))z}\right]I_{2m}. \end{aligned} \tag{2.5}$$

where

$$\begin{aligned} I_{1m} &= 2\pi\int_0^{a_1}\vec{E}_{co}^{*}(\vec{r})\vec{E}_m(\vec{r})rdr, \\ I_{2m} &= 2\pi\int_{a_1}^{a_2}\vec{E}_{co}^{*}(\vec{r})\vec{E}_m(\vec{r})rdr. \end{aligned} \tag{2.6}$$

The detuning parameter is shown in Equation (2.5)

$$\Delta = \frac{2\pi}{\Lambda} \pm (\beta_{co} - \beta_m). \tag{2.7}$$

For a coupling from LP_{01} core mode to a forward-propagating cladding mode, the term with $2\pi/\Lambda + (\beta_{co} - \beta_m)$ can be neglected.

The analytical solution of Equations (2.1) and (2.2) is [23]

$$A_{co}(z) = A_1 \cos\left(\sqrt{\left(\frac{\Delta}{2}\right)^2 + \left|C_{co-m}\right|^2}\, z\right) e^{-i\frac{\Delta}{2}z} + B_1 \sin\left(\sqrt{\left(\frac{\Delta}{2}\right)^2 + \left|C_{co-m}\right|^2}\, z\right) e^{-i\frac{\Delta}{2}z}, \quad (2.8)$$

$$B_m(z) = A_2 \cos\left(\sqrt{\left(\frac{\Delta}{2}\right)^2 + \left|C_{co-m}\right|^2}\, z\right) e^{i\frac{\Delta}{2}z} + B_2 \sin\left(\sqrt{\left(\frac{\Delta}{2}\right)^2 + \left|C_{co-m}\right|^2}\, z\right) e^{i\frac{\Delta}{2}z}. \quad (2.9)$$

where the detuning parameter

$$\Delta = \frac{2\pi}{\Lambda} - (\beta_{co} - \beta_m). \quad (2.10)$$

Applying the boundary conditions $A_{co}(0) = 1, B_m(0) = 0$, Equations (2.8) and (2.9) are reduced to

$$A_{co}(z) = \left[\begin{array}{l} \cos\left(\sqrt{\left(\frac{\Delta}{2}\right)^2 + \left|C_{co-m}\right|^2}\, z\right) + \\ i\dfrac{\Delta}{2\sqrt{\left(\frac{\Delta}{2}\right)^2 + \left|C_{co-m}\right|^2}} \sin\left(\sqrt{\left(\frac{\Delta}{2}\right)^2 + \left|C_{co-m}\right|^2}\, z\right) \end{array}\right] e^{-i\frac{\Delta}{2}z}, \quad (2.11)$$

$$B_m(z) = i\frac{C_{co-m}}{\sqrt{\left(\frac{\Delta}{2}\right)^2 + \left|C_{co-m}\right|^2}} \sin\left(\sqrt{\left(\frac{\Delta}{2}\right)^2 + \left|C_{co-m}\right|^2}\, z\right) e^{i\frac{\Delta}{2}z-\phi}. \quad (2.12)$$

Thus, the transmittance is

$$T_{co-z} = \cos^2\left(\sqrt{\left(\frac{\Delta}{2}\right)^2 + \left|C_{co-m}\right|^2}\, z\right) + \frac{\left(\frac{\Delta}{2}\right)^2}{\left(\frac{\Delta}{2}\right)^2 + \left|C_{co-m}\right|^2} \sin^2\left(\sqrt{\left(\frac{\Delta}{2}\right)^2 + \left|C_{co-m}\right|^2}\, z\right). \quad (2.13)$$

Under the phase matching condition

$$\Delta = \frac{2\pi}{\Lambda} - (\beta_{co} - \beta_m) = 0. \quad (2.14)$$

The transmittance is changed to

$$T_{co-z} = \cos^2\left(\left|C_{co-m}\right| z\right). \quad (2.15)$$

with a full conversion at

$$z = \frac{\pi}{2|C_{co-m}|}. \tag{2.16}$$

The modeling of LPG requires the calculation of the effective refractive index of core and cladding modes. The resonant wavelength of an attenuation band in the transmission spectrum is determined by the phase matching condition in Equation (2.14). The coupling coefficient is related to the mode overlap and refractive index modulation and distribution. The mode coupling theory also applies to FBGs with the situation of counter-direction coupling due to the small period Λ. In the case of conversion between forward LP_{01} mode and backward LP_{01} mode, the corresponding phase matching condition is

$$2\beta_{co} = \frac{2\pi}{\Lambda}. \tag{2.17}$$

2.3 Long-period grating sensors

Fiber grating is widely used in the realm of sensing. It has response to local environment such as temperature, strain or pressure. Compared to FBGs, an LPG is more sensitive to temperature and ambient refractive index [35]. The coupling from fundamental core mode to cladding modes is determined by the grating period, effective index of core and cladding modes that are affected by temperature, strain and the refractive index of the external medium. A complete expression of the shift of resonant wavelength relating to the temperature, strain and external refractive index changes is given by as [23]:

$$\Delta\lambda_{res} = (\frac{d\lambda_{res}}{dT})\Delta T + (\frac{d\lambda_{res}}{dS})\Delta S + (\frac{d\lambda_{res}}{dn_{ext}})\Delta n_{ext}. \tag{2.18}$$

where $d\lambda_{res}/dT$, $d\lambda_{res}/dS$ and $d\lambda_{res}/dn_{ext}$ are the temperature, strain and ambient refractive index sensitivities of the resonant wavelength, respectively. A detailed expression for the sensitivities will be presented in the next section.

2.3.1 Temperature sensing

For a traditional LPG fiber sensor, the temperature variation will change the effective index of core and cladding modes and the difference between them, therefore the resonant wavelength will shift according to the phase matching condition (Equation

(2.14)). The expression for the temperature sensitivity of an LPG can be expressed as [36]:

$$\frac{d\lambda_{res}}{dT} = \lambda_{res}\gamma(\alpha + \frac{\xi_{co}n_{co}^{eff} - \xi_{cl}n_{cl,m}^{eff}}{n_{co}^{eff} - n_{cl,m}^{eff}}). \tag{2.19}$$

with

$$\gamma = \frac{d\lambda_{res} / d\Lambda}{n_{co}^{eff} - n_{cl,m}^{eff}}. \tag{2.20}$$

where λ_{res} is the center wavelength, α is the thermal expansion coefficient of the fiber, ξ_{co}, ζ_{cl} are the thermo-optic coefficients of core and cladding materials. T is the temperature, n_{co}^{eff} is the effective index of the core mode, $n_{cl,m}^{eff}$ is the effective index of the cladding mode, Λ is the LPG period. A typical temperature response is shown in Figure 2-4(a) which gives the shift of a certain attenuation band at temperatures 22.7, 49.1, 74.0, 100.9, 127.3 and 149.7 ℃ (correspond to the lines from left to right) for a Corning SMF28 fiber with a period of 280 μm. The linearity of temperature response is shown in Figure 2-4(b) for different attenuation bands at temperature from 30 to 150 ℃. It is noticed that the temperature response is not always linear, it has been shown that the response becomes nonlinear at cryogenic temperatures below 77K [37].

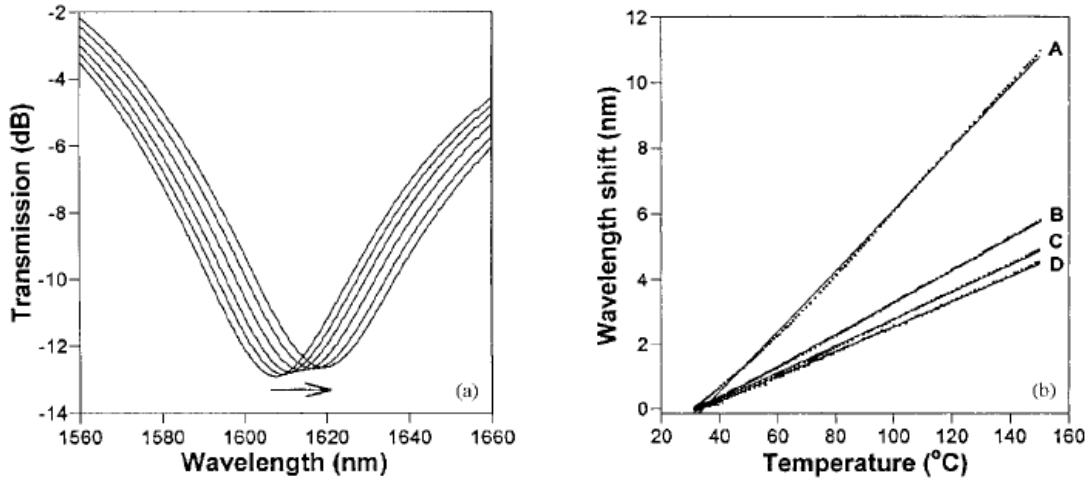

(a) (b)

Figure 2-4 (a) Wavelength shift of an LPG at different temperatures (from left to right): 22.7, 49.1, 74.0, 100.9, 127.3 and 149.7 ℃. (b) Wavelength shift for various resonant bands (at 31.2 ℃) A: 1608.6 nm, B: 1332.9 nm, C: 1219.7 nm and D: 1159.6 nm [38].

2.3.2 Strain sensing

Like the expression for temperature sensitivity, the strain sensitivity of LPGs is expressed as [36]

$$\frac{d\lambda_{res}}{d\varepsilon} = \lambda_{res}\gamma(1+\frac{\eta_{co}n_{co}^{eff} - \eta_{cl}n_{cl,m}^{eff}}{n_{co}^{eff} - n_{cl,m}^{eff}}). \tag{2.21}$$

where η_{co}, η_{cl} are the elasto-optic coefficients of core and cladding materials. A typical axial strain response is illustrated in Figure 2-5 for a 280 μm LPG written in Corning SMF28 fiber. Linear response is seen for four different attenuation bands. In additional to axial strain, the sensitivity of LPGs to transverse strains has been investigated as well [39].

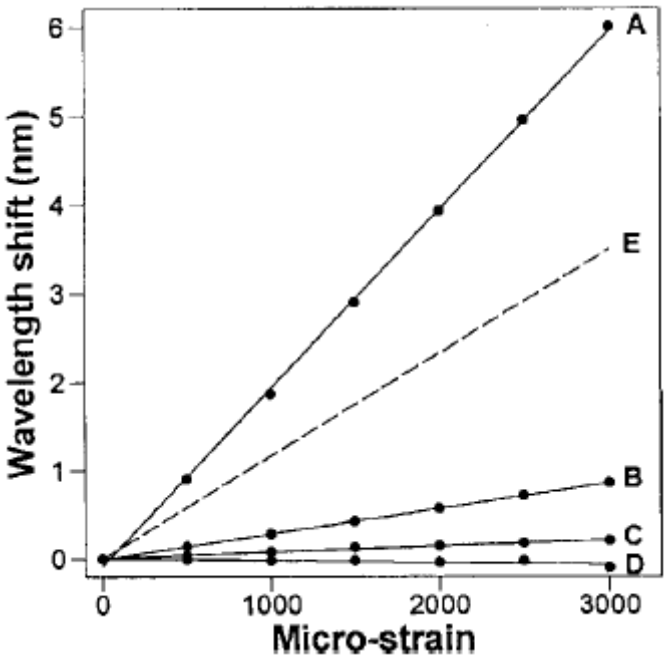

Figure 2-5 Wavelength shift for four attenuation bands A: 1607.8 nm, B: 1332.4 nm, C: 1219.3 nm and D: 1159.3 nm (at no strain) as a function of strain. The dashed line represents the shift for a Bragg grating fabricated at 1550 nm [38] as a comparison.

2.3.3 Refractive index sensing

Since the change of the refractive index of ambient medium will vary the effective refractive index of the cladding mode and the effective refractive index difference

$\beta_{co} - \beta_m$. The resonant wavelength will shift when ambient index varies. The refractive index sensitivity depends on the refractive index of the core, cladding and external ambient medium with an expression of [36]

$$\frac{d\lambda_{nes}}{dn_{sur}} = -\gamma\lambda_{nes}\left(\frac{u_m^2\lambda_{res}^3 n_{sur}}{8\pi r_{cl}^3 n_{cl}\left(n_{co}^{eff} - n_{cl,m}^{eff}\right)\left(n_{cl}^2 - n_{sur}^2\right)^{3/2}}\right). \tag{2.22}$$

where u_m is the m[th] root of the zero-order Bessel function, r_{cl}, n_{cl} are the radius and refractive index of the fiber cladding, respectively. Figure 2-6 shows the external refractive index induced band shift for a LPG with a length of 40 mm, period of 400 μm fabricated in a B-Ge co-doped fiber (Fibercore PS750). Refractive index sensitivity becomes manifest during the range of 1.400-1.460, and disappears after 1.46 which closes to the limit of cladding mode. From Equation (2.22) it is seen that the refractive index is more evident for high order cladding modes and reduced cladding radius [40].

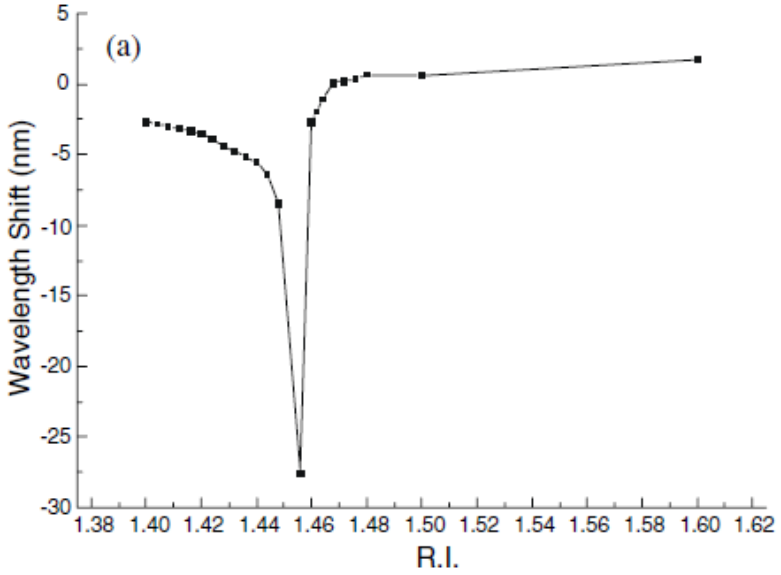

Figure 2-6 Wavelength shift of an attenuation band as a function of ambient refractive index for a LPG of 400 μm written in a B-Ge co-doped fiber with a cut off wavelength of 650 μm [41].

2.3.4 Bend sensing

The bending of the LPG usually brings two effects: the shift of resonant wavelength and the split of attenuation band. It has been observed that the shift of resonant wavelength, which can be explained by the change of LPG period due to bending, is accompanied by a reduction in the loss and a broadening of the spectrum [42]. The splitting of attenuation band has been observed in a B-Ge co-doped fiber [43] and a fiber with large core concentricity error [44]. An explanation for the splitting is the break of symmetry between the two normally degenerate spatial cladding modes that introduce a refractive index difference between them. Figure 2-7 demonstrates the effect of bending to the shift of resonant wavelength and the splitting of attenuation band for a LPG of length 40 mm, period of 400 μm, inscribed in a B-Ge co-doped fiber. At no curvature, there is one band centered at around 1010 nm. When bending the fiber to 1.55 m^{-1}, the one band splits into two bands located at 990 nm and 1030 nm separately. The exact theoretical analysis of bending sensitivity is very complex and needs further work.

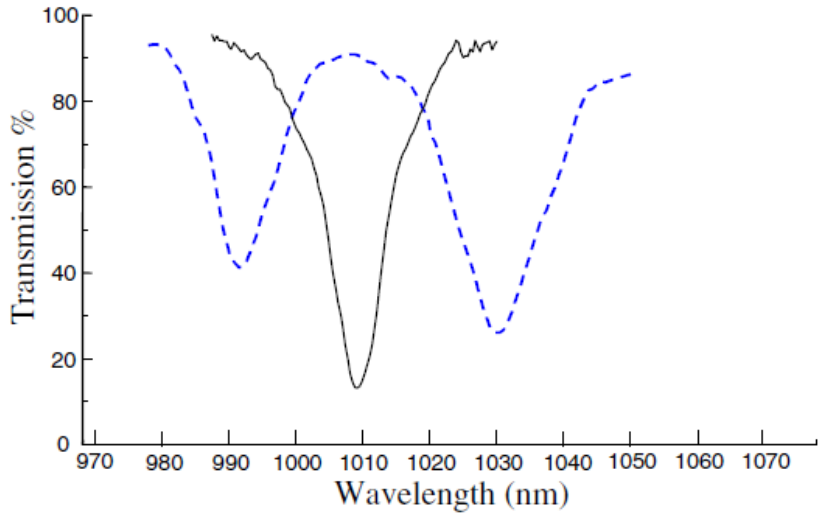

Figure 2-7 Transmission spectrum for one attenuation band of a 400 μm-period LPG at curvature 0 m^{-1} (solid curve) and 1.55 m^{-1} (dashed curve). The LPG was inscribed in a B-Ge co-doped fiber [45].

Chapter 3

Theory and numerical analysis of OLPG-based Fiber Sensors

In Chapter 2, traditional LPGs are introduced from the fabrication process, coupled mode theory to the sensing applications. Chapter 3 will focus on the detailed theoretical analysis of OLPG-based fiber sensors. Numerical simulation is provided to model both core-core and core-cladding mode conversions. The application of OLPG to fiber sensors is also analyzed and the sensitivity to temperature, axial strain and refractive index is calculated.

The outline of Chapter 3 is as follows. Section 3.1 provides the principle of OLPG-based fiber sensors. Section 3.2 focuses on the numerical simulation of mode conversion in an OLPG. Sections 3.3 - 3.5 discuss the sensing applications and calculate the sensitivity of OLPG as a function of temperature, axial strain and refractive index. The difference between an OLPG and an LPG is also analyzed. The analysis shows that the grating period response is different for temperature and axial strain sensors. Section 3.6 introduces a possible system of the OLPG-based distributed fiber sensors, and Section 3.7 analyzes the sensing system including the drawbacks and limitations of the system, how to move the resonant wavelength into C-band that can be covered by a common tunable laser and the effect of the writing power as well as the power distribution.

3.1 Principle of OLPG-based fiber sensors

In the scheme of OLPG-based fiber sensors, a high power pulsed beam, which is called a writing beam, is launched into a few mode fiber. After careful tuning, two modes are generated (usually LP_{01} and LP_{11}) to co-propagate through the few mode fiber. As the two modes have different propagation constants, a beating will be formed with a period of $2\pi/(\beta_{01}-\beta_{11})$. Due to the optical Kerr effect, periodic refractive index perturbation (grating) is hence generated with the same period and a length same as the pulse width. Compared to the acoustically induced LPG, this LPG is called optically induced LPG (OLPG).

After the formation of OLPG, a continuous counter-propagating beam, which is called a probe beam, is launched into the few mode fiber at a different wavelength. Careful alignment is necessary to make sure the probe beam only excites LP_{01} core mode. When the probe beam encounters the refractive index perturbation and the phase matching condition is satisfied, mode conversion will occur from the core mode to a cladding mode like the traditional LPG.

It is noticed that since the LPG is formed by the beating of two co-propagating core modes, its response to local environment (temperature, strain and ambient refractive index) is different from a traditional LPG. In the case of temperature sensing, the change of temperature induces the change of refractive indices of the core and cladding and hence the effective indices of the two core modes. Since the OLPG period is determined by the difference of propagation constants between the two core modes, the strain and temperature factors will exert subtle effect on the period. However, the period is sensitive to the refractive index of the ambient medium due to its influence on the effective refractive index of the cladding mode.

Distributed sensing is obtained from the time-domain signal of the transmitted probe beam. In order to observe the resonant bands, the source for the probe beam needs to have a spectrum covering the resonant wavelengths. In the case of traditional LPG sensing, a continuous broadband source is used as a probe beam and the resonant wavelength can be observed through the transmission spectrum. However, in the case of OLPG distributed sensing, the pulse width is usually very small (~10 ns) with a large period (~0.1s), and the mode conversion only occurs within the duration of the pulse width. So a fast oscilloscope is needed in order to observe the mode conversion (attenuation) within ~10 ns for each fixed wavelength of the probe beam. Moreover, a wavelength scan of the probe beam is needed to obtain the resonant wavelengths. The source for the probe beam should be a tunable laser with a tuning range covering the resonant bands.

3.2 Numerical simulation

This section focuses on the numerical simulation of mode conversion in an OLPG. In Section 3.2.1, a numerical tool - finite-difference beam propagation method (FD-BPM) is introduced to simulate the mode propagation in the OLPG, along with the perfectly matched layers (PML) boundary condition. The use of BPM is due to its advantage to deal with complex waveguide structures and random transverse refractive index distribution. Sections 3.2.2 and 3.2.3 demonstrate the simulation of both core-core and core-cladding mode coupling based on BPM. The result shows that full conversion can be observed when phase matching condition is satisfied. When the probe laser wavelength is scanned over a spectral range from 1.2 μm to 1.9 μm, several resonant bands may be observed, corresponding to the coupling between LP_{01} core mode and different LP_{1m} cladding modes.

3.2.1 Finite-difference beam propagation method

Beam propagation method (BPM) is one of the most widely used numerical methods to simulate the guided wave propagation in an inhomogeneous medium. Feit and Fleck first applied it to fiber optics to calculate the mode properties [46, 47]. Since then many other structures such as gratings [48], waveguide crossings [49] and fiber couplers [50] have been modeled by the BPM.

The idea of conventional BPM is to represent the electromagnetic field by the superposition of plane waves in homogeneous media. For the propagation in inhomogeneous media, the wave is modeled as an integral of plane waves in the spectral domain with a phase correction added after each propagation step. The FFT is used to connect between the spatial and the spectral domains, hence the method is called split-operator FFT-BPM which can be expressed as [51]:

$$\psi(x, y, z + \Delta z) = PQP\psi(x, y, z). \tag{3.1}$$

where $\psi(x, y, z)$ and $\psi(x, y, z + \Delta z)$ are field distributions at two subsequent propagation steps, P is a propagator which can be solved by FFT and Q is a phase correction.

Recently finite-difference beam propagation method (FD-BPM) is widely used over the previous FFT-BPM to improve the efficiency and flexibility [51]. In the next part,

mathematical derivation of paraxial and wide-angle wave equations for finite-difference vectorial beam propagation method are given, along with the numerical scheme for FD-BPM.

3.2.1.1. Derivation of Vectorial Helmholtz Equations [51]

Maxwell's equations in linear and isotropic media are written as:

$$\nabla \times \vec{E} = -j\omega\mu_0 \vec{H}, \tag{3.2}$$

$$\nabla \times \vec{H} = j\omega n^2 \varepsilon_0 \vec{E}. \tag{3.3}$$

Take the curl of Equation (3.2) and use Equation (3.3),

$$\nabla \times \nabla \times \vec{E} - n^2 k_0^2 \vec{E} = 0. \tag{3.4}$$

By using $\nabla \times \nabla \times = \nabla(\nabla \cdot) - \nabla^2$, Equation (3.4) is changed to

$$\nabla^2 \vec{E} + n^2 k_0^2 \vec{E} = \nabla(\nabla \cdot \vec{E}). \tag{3.5}$$

Consider the transverse fields,

$$\nabla^2 \vec{E}_t + n^2 k_0^2 \vec{E}_t = \nabla_t (\nabla_t \cdot \vec{E}_t + \frac{\partial E_z}{\partial z}). \tag{3.6}$$

where 't' represents the transverse components.

From Gauss's law,

$$\nabla \cdot (n^2 \vec{E}_t) = 0. \tag{3.7}$$

which is transformed to

$$\nabla_t \cdot (n^2 \vec{E}_t) + \frac{\partial n^2}{\partial z} E_z + n^2 \frac{\partial E_z}{\partial z} = 0. \tag{3.8}$$

For a slow variation of refractive index in propagation direction z, which applies to most guided waves, the term $\frac{\partial n^2}{\partial z} E_z$ can be negligible. Thus,

$$\frac{\partial E_z}{\partial z} \approx -\frac{1}{n^2} \nabla_t \cdot (n^2 \vec{E}_t). \tag{3.9}$$

Substituting Equation (3.9) into Equation (3.6), we obtain the vectorial Helmholtz equation based on the transverse electric fields

$$\nabla^2 \vec{E}_t + n^2 k_0^2 \vec{E}_t = \nabla_t (\nabla_t \cdot \vec{E}_t - \frac{1}{n^2} \nabla_t \cdot (n^2 \vec{E}_t)). \tag{3.10}$$

Same procedure can be applied to transverse magnetic fields with

$$\nabla^2 \vec{H}_t + n^2 k_0^2 \vec{H}_t = -\frac{1}{n^2} \nabla_t n^2 \times (\nabla_t \times \vec{H}_t). \tag{3.11}$$

3.2.1.2. One-way wave equations

Assuming the wave propagates in +z direction, the field can be separated as

$$\vec{E}_t(x, y, z) = E_t(x, y, z) e^{-jn_r k_0 z}, \tag{3.12}$$

where n_r is a reference index that should be chosen close to the effective index such that the envelop varies slowly. Substitute Equation (3.12) into Equation (3.10) to obtain one-way wave equation

$$\frac{\partial}{\partial z}\left(j2n_r k - \frac{\partial}{\partial z} \right) E_t = PE_t. \tag{3.13}$$

where the operator P satisfies

$$PE_t = \nabla_t^2 E_t + (n^2 - n_r^2) k_0^2 E_t - \nabla_t \left[\nabla_t \cdot E_t - \frac{1}{n^2} \nabla_t \cdot (n^2 E_t) \right]. \tag{3.14}$$

or

$$P_{xx} E_x = \frac{\partial}{\partial x}\left[\frac{1}{n^2} \frac{\partial (n^2 E_x)}{\partial x} \right] + \frac{\partial^2 E_x}{\partial y^2} + k_0^2 (n^2 - n_r^2) E_x, \tag{3.15}$$

$$P_{yy} E_y = \frac{\partial^2 E_y}{\partial x^2} + \frac{\partial}{\partial y}\left[\frac{1}{n^2} \frac{\partial (n^2 E_y)}{\partial y} \right] + k_0^2 (n^2 - n_r^2) E_y, \tag{3.16}$$

$$P_{xy} E_y = \frac{\partial}{\partial x}\left[\frac{1}{n^2} \frac{\partial (n^2 E_y)}{\partial y} \right] - \frac{\partial^2 E_y}{\partial x \partial y}, \tag{3.17}$$

$$P_{yx} E_x = \frac{\partial}{\partial y}\left[\frac{1}{n^2} \frac{\partial (n^2 E_x)}{\partial x} \right] - \frac{\partial^2 E_x}{\partial y \partial x}. \tag{3.18}$$

here

$$P = \begin{bmatrix} P_{xx} & P_{xy} \\ P_{yx} & P_{yy} \end{bmatrix}. \tag{3.19}$$

Similarly for transverse magnetic fields,

$$\frac{\partial}{\partial z}\left(j2n_r k - \frac{\partial}{\partial z}\right) H_t = QH_t. \tag{3.20}$$

where the operator Q satisfies

$$Q_{xx}H_x = \frac{\partial^2 H_x}{\partial x^2} + n^2 \frac{\partial}{\partial y}\left(\frac{1}{n^2}\frac{\partial H_x}{\partial y}\right) + k_0^2 (n^2 - n_r^2)E_x, \tag{3.21}$$

$$Q_{yy}H_y = \frac{\partial^2 H_y}{\partial y^2} + n^2 \frac{\partial}{\partial x}\left(\frac{1}{n^2}\frac{\partial H_y}{\partial x}\right) + k_0^2 (n^2 - n_r^2)H_y, \tag{3.22}$$

$$Q_{xy}H_y = \frac{\partial^2 H_y}{\partial y \partial x} - n^2 \frac{\partial}{\partial y}\left(\frac{1}{n^2}\frac{\partial H_y}{\partial x}\right), \tag{3.23}$$

$$Q_{yx}H_x = \frac{\partial^2 H_x}{\partial x \partial y} - n^2 \frac{\partial}{\partial x}\left(\frac{1}{n^2}\frac{\partial H_x}{\partial y}\right). \tag{3.24}$$

3.2.1.3. Wave equations for paraxial and wide-angle conditions

The paraxial and wide-angle wave equations are obtained by applying the Pade approximation [51]

$$\left.\frac{\partial}{\partial z}\right|_{i+1} = \frac{P}{j2n_r k_0 - \left.\frac{\partial}{\partial z}\right|_i}. \tag{3.25}$$

with $\left.\frac{\partial}{\partial z}\right|_0 = 0$.

Let i = 1 to derive the paraxial equation

$$j2n_r k_0 \frac{\partial E_t}{\partial z} = PE_t. \tag{3.26}$$

Let i = 2 to obtain the first-order wide-angle wave equation

$$j\left(2n_r k_0 + \frac{P}{2n_r k_0}\right)\frac{\partial E_t}{\partial z} = PE_t. \tag{3.27}$$

3.2.1.4. Semi-vectorial and Scalar wave equations

If the coupling between two polarizations is weak, a semi-vectorial wave equation is derived. Neglect the terms P_{xy} and P_{yx} to have

Paraxial:

$$j2n_r k_0 \frac{\partial E_x}{\partial z} = P_{xx}E_x, \tag{3.28}$$

$$j2n_r k_0 \frac{\partial E_y}{\partial z} = P_{yy}E_y. \tag{3.29}$$

Wide-angle:

$$j\left(2n_r k_0 + \frac{P_{xx}}{2n_r k_0}\right)\frac{\partial E_x}{\partial z} = P_{xx}E_x. \tag{3.30}$$

$$j\left(2n_r k_0 + \frac{P_{yy}}{2n_r k_0}\right)\frac{\partial E_y}{\partial z} = P_{yy}E_y. \tag{3.31}$$

Corresponding equations for magnetic fields are obtained by replacing P_{xx}, P_{yy}, E_x and E_y by Q_{xx}, Q_{yy}, H_x and H_y, respectively.

For weakly-guiding structures, even the polarization dependence may be neglected. The scalar approximation is obtained by letting

$$P = P_{xx} = P_{yy} = Q_{xx} = Q_{yy} = \frac{\partial^2}{\partial x^2} + \frac{\partial^2}{\partial y^2} + k_0^2 (n^2 - n_r^2). \tag{3.32}$$

3.2.1.5. Finite-difference discretization

Let $E_x(i, j), E_y(i, j)$ and $n_{i,j}$ represent the electric fields and the refractive index at the mesh (i, j). Equations (3.15)-(3.18) can be discretized as:

$$\begin{aligned} P_{xx}E_x = & \frac{M^x_{i+1,j}E_x(i+1, j) - M^x_{i,j}E_x(i, j) + M^x_{i-1,j}E_x(i-1, j)}{(\Delta x)^2} \\ & + \frac{E_x(i, j+1) - 2E_x(i, j) + E_x(i, j-1)}{(\Delta y)^2} + (n^2_{i,j} - n_r^2)k_0^2 E_x(i, j). \end{aligned} \tag{3.33}$$

with

$$\begin{aligned} M^x_{i\pm1,j} &= \frac{n^2_{i\pm1,j} + n^2_{i,j}}{2n^2_{i,j}}, \\ M^x_{i,j} &= \frac{n^2_{i-1,j} + n^2_{i,j}}{2n^2_{i-1,j}} + \frac{n^2_{i+1,j} + n^2_{i,j}}{2n^2_{i+1,j}}. \end{aligned} \tag{3.34}$$

and

$$\begin{aligned} P_{yy}E_y = & \frac{M^y_{i,j+1}E_y(i, j+1) - M^y_{i,j}E_y(i, j) + M^y_{i,j-1}E_y(i, j-1)}{(\Delta y)^2} \\ & + \frac{E_y(i+1, j) - 2E_y(i, j) + E_y(i-1, j)}{(\Delta x)^2} + (n^2_{i,j} - n_r^2)k_0^2 E_y(i, j). \end{aligned} \tag{3.35}$$

with

$$\begin{aligned} M^y_{i,j\pm1} &= \frac{n^2_{i,j\pm1} + n^2_{i,j}}{2n^2_{i,j}}, \\ M^y_{i,j} &= \frac{n^2_{i,j-1} + n^2_{i,j}}{2n^2_{i,j-1}} + \frac{n^2_{i,j+1} + n^2_{i,j}}{2n^2_{i,j+1}}. \end{aligned} \tag{3.36}$$

and

$$P_{xy}E_y = \frac{1}{4\Delta x\Delta y}\left\{\left[\frac{n^2_{i+1,j+1}}{n^2_{i+1,j}}-1\right]E_y(i+1,j+1)-\left[\frac{n^2_{i+1,j-1}}{n^2_{i+1,j}}-1\right]E_y(i+1,j-1)\right.$$
$$\left.-\left[\frac{n^2_{i-1,j+1}}{n^2_{i-1,j}}-1\right]E_y(i-1,j+1)+\left[\frac{n^2_{i-1,j-1}}{n^2_{i-1,j}}-1\right]E_y(i-1,j-1)\right\}, \tag{3.37}$$

$$P_{yx}E_x = \frac{1}{4\Delta x\Delta y}\left\{\left[\frac{n^2_{i+1,j+1}}{n^2_{i,j+1}}-1\right]E_x(i+1,j+1)-\left[\frac{n^2_{i-1,j+1}}{n^2_{i,j+1}}-1\right]E_x(i-1,j+1)\right.$$
$$\left.-\left[\frac{n^2_{i+1,j-1}}{n^2_{i,j-1}}-1\right]E_x(i+1,j-1)+\left[\frac{n^2_{i-1,j-1}}{n^2_{i,j-1}}-1\right]E_x(i-1,j-1)\right\}. \tag{3.38}$$

The transverse magnetic fields can be discretized in the same way.

3.2.1.6. Numerical scheme for FD-BPM

The solution for Equation (3.26) with an exponential form is

$$E_t(x,y,z+\Delta z) = e^{-jP\Delta z}E_t(x,y,z), \tag{3.39}$$

We can also write it as a weighted finite-difference form

$$E_t(x,y,z+\Delta z) = \frac{2n_r k_0 - j\Delta z(1-\alpha)P}{2n_r k_0 + j\Delta z\alpha P}E_t(x,y,z). \tag{3.40}$$

where Δz is the longitudinal step size and α is a weighting factor that affects the stability, the numerical dissipation and dispersion [51]. α = 1 corresponds to the standard implicit scheme and α = 0 explicit. α = 0.5 is the Crank-Nicholson scheme. The discretization of Equation (3.40) yields a matrix equation

$$A\left[E_t\right]^{m+1} = B\left[E_t\right]^m. \tag{3.41}$$

where $\left[E_t\right]^{m+1}$ and $\left[E_t\right]^m$ are the fields at two sequential steps. A and B are matrices obtained from the operator P. The matrix A has 9 none-zero elements for the 3-D full-vectorial equations and 5 none-zero elements for the 3-D semi-vectorial and scalar equations. For 2-D structures, A is reduced to a tri-diagonal matrix that can be inverted by the LU solver.

3.2.1.7. Boundary conditions

The choice of boundary conditions is very essential in numerical simulation. Several techniques have been used to avoid the reflection by the boundaries. A conventional method is the absorbing boundary condition (ABC) in which an artificial layer with lossy media is added to surround the computational area. By properly choosing the absorption coefficients and the layer thickness, the out-going wave is attenuated before reaching the boundary edge. The disadvantage of ABC is its problem-dependence. Another technique is the transparent boundary condition (TBC) [52] which lets a quasi-plane wave pass at a particular incident angle. Compared to ABC, TBC technique is problem-independent and more robust. However, TBC still has limitations, especially for the simulation of wide-angle propagation waves. After TBC, a more effective boundary condition - perfectly matched layer (PML) has been widely used since it was proposed by Berenger [53] in 1994. After implementing PML, the Maxwell's equations are written as [54]

$$\nabla' \times \vec{H} = j\omega\varepsilon_0 n^2 s\vec{E}, \tag{3.42}$$

$$\nabla' \times \vec{E} = -j\omega\mu_0 s\vec{H}. \tag{3.43}$$

with

$$s = 1 - j\frac{\sigma_e}{\omega\varepsilon_0 n^2} = 1 - j\frac{\sigma_m}{\omega\mu_0}. \tag{3.44}$$

where σ_e, σ_m are the electric and magnetic conductivities of PML, respectively. The modified differential operator ∇' is defined as

$$\nabla' = \nabla_t' + \vec{e}_z \nabla_z', \tag{3.45}$$

with

$$\begin{aligned} \nabla_t' &= \vec{e}_x s_x \frac{\partial}{\partial x} + \vec{e}_y s_y \frac{\partial}{\partial y}, \\ \nabla_z' &= s\frac{\partial}{\partial z}. \end{aligned} \tag{3.46}$$

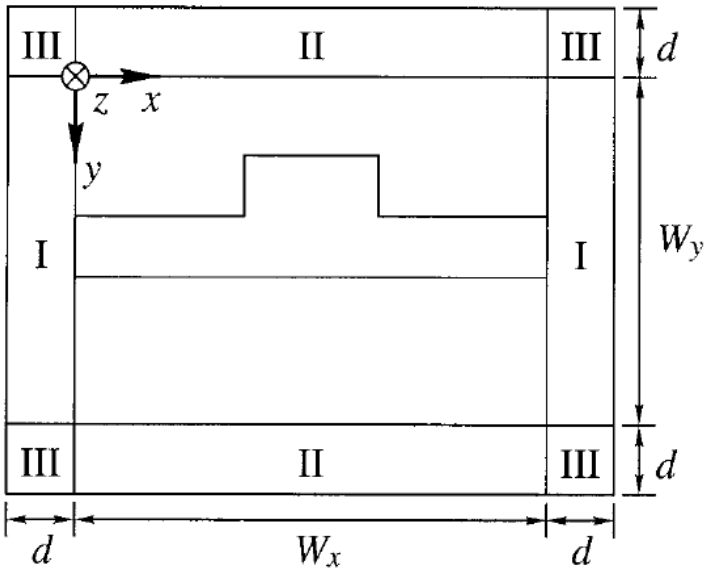

Figure 3-1 Computation area surrounded by PML [55].

Figure 3-1 shows a PML structure in a transverse computation area. The values of s_x, s_y are different in different areas

$$\begin{aligned} &s_x = 1, s_y = s \quad \text{Region I} \\ &s_x = s, s_y = 1 \quad \text{Region II} \\ &s_x = 1, s_y = 1 \quad \text{Region III} \end{aligned} \tag{3.47}$$

The PML impedance matching condition requires

$$\frac{\sigma_e}{\varepsilon_0 n^2} = \frac{\sigma_m}{\mu_0}. \tag{3.48}$$

In the PML, we assume a m^{th} power profile of electric conductivity

$$\sigma_e = \sigma_{\max} (\frac{\rho}{d})^m. \tag{3.49}$$

with

$$\sigma_{\max} = \frac{m+1}{2} \frac{\varepsilon_0 cn}{d} \ln \frac{1}{R}. \tag{3.50}$$

where ρ is the distance from the beginning of PML, d is the total thickness of PML, R is the theoretical reflection coefficient. Usually a small R (10^{-7}) is assumed to make sure nearly no reflection by PML.

3.2.2 Simulation of core-core mode conversion

In order to verify the effect of OLPG, the core-core mode conversion is simulated using the 3D scalar beam propagation method with perfectly matched layer boundary condition. The modeled few mode optical fiber is the Corning SMF28 with a core width of 8 μm and cladding diameter of 125 μm. The refractive index of the core is 1.45435, and the cladding is 1.44963 at 1064 nm. Assume a high power Q-switched Nd:YAG laser (writing beam) propagates through the fiber. At 1064 nm, dual modes (LP_{01} and LP_{11}) exist and form a traveling long-period grating through mode interference. Based on the above parameters, the calculated grating period is 444 μm. The perturbed refractive index profile is constructed by obtaining the mode interference pattern and using the Kerr induced index change $\Delta n = n_2 I$, where the nonlinear index n_2 is chosen to be $2.6\times10^{-20}\,\mathrm{m}^2/\mathrm{W}$ for silica fiber. In order to simplify the problem, the LP_{01} mode is assumed to be x-polarized as well as the LP_{11} mode. Furthermore, assume LP_{11} mode have a $\cos\varphi$ azimuthal term. Thus, we can represent the electric fields of the two modes in the core as

$$\begin{aligned} \vec{E}_{01} &= \hat{x} J_0\left(k_{\perp 01} r\right), \\ \vec{E}_{11} &= \hat{x} J_1\left(k_{\perp 11} r\right)\cos\varphi. \end{aligned} \tag{3.51}$$

with corresponding field profiles shown in Figure 3-2.

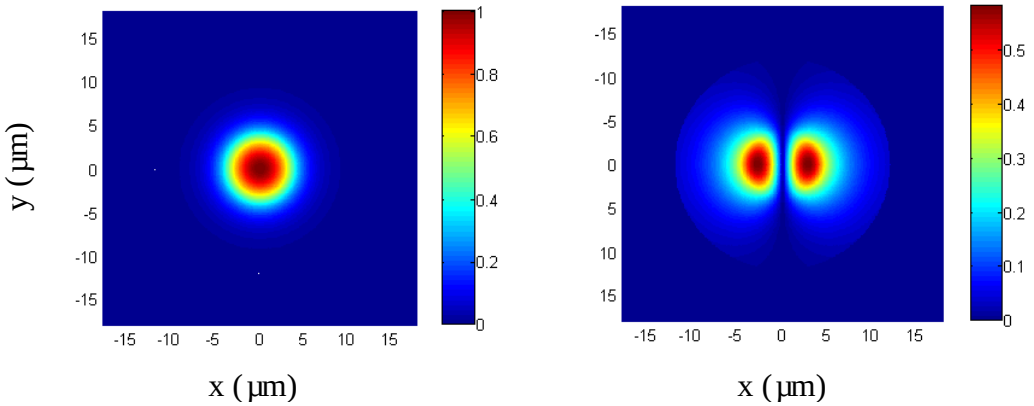

Figure 3-2 Electric fields of LP_{01} and LP_{11} modes. Both are x-polarized.

Figure 3-3 shows the optically induced refractive index modulation due to the interference of the two modes when a total launched power is 200 kW with 50% of the

power in LP_{01} mode as well as in the LP_{11} mode. Since the LP_{11} mode has a $\cos\varphi$ azimuthal term, there is no refractive index modulation in y-cut plane (x = 0). However, in the x-cut plane (y = 0), a periodic refractive index modulation is clearly seen with a period of 444 μm. Moreover, it is noticed that the distribution of the refractive index modulation is not circularly symmetric ($\Delta n(\vec{r},\varphi)$ is dependent on azimuthal term φ), which is not the case for the refractive index profile in traditional LPG. This is also the reason why the BPM is implemented for the modeling instead of commercial software like Optiwave which cannot solve the situation with asymmetric index perturbation.

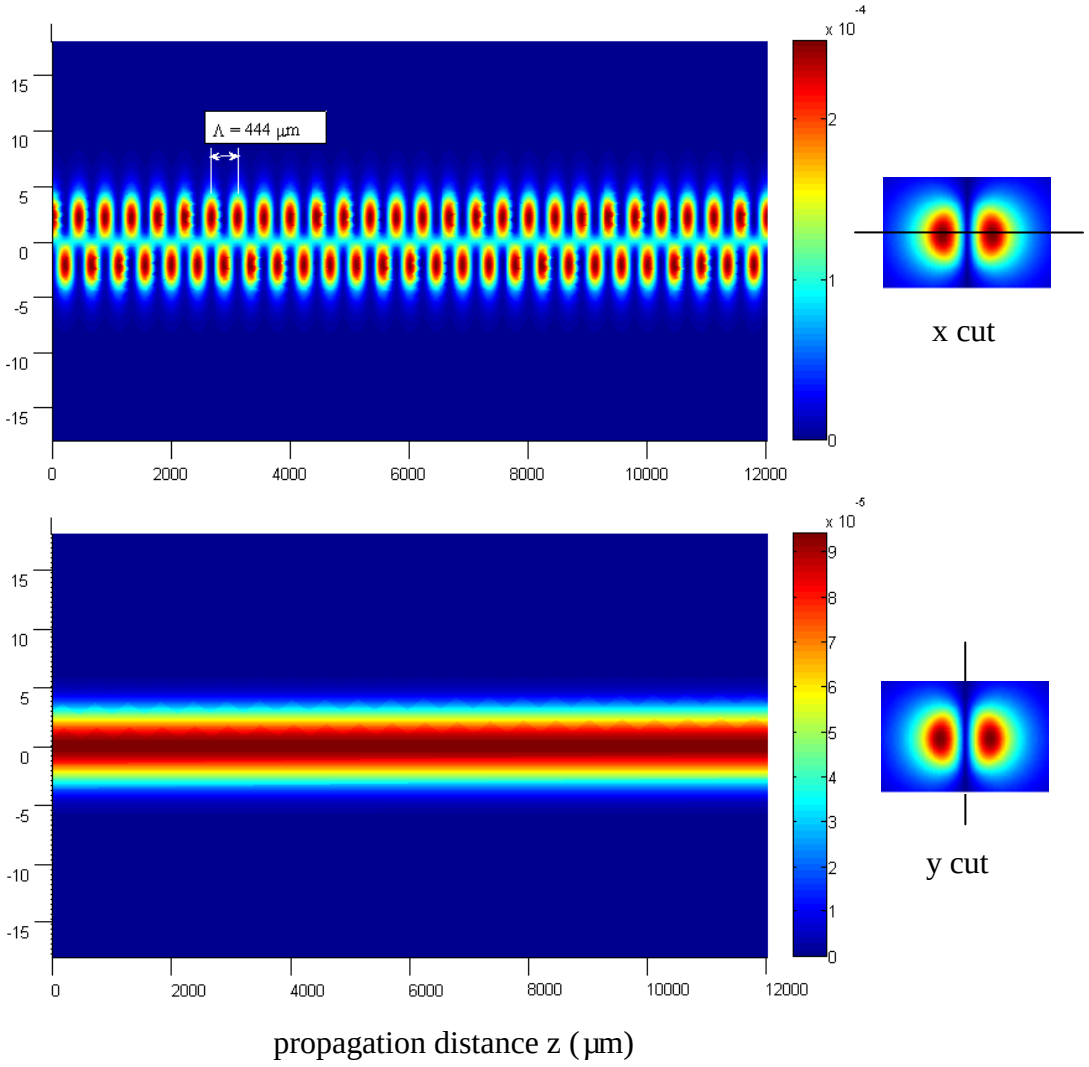

Figure 3-3 Profile of optically induced refractive index perturbation. The total launched power is 200 kW and 50% of the power is in LP_{01} mode as well as in LP_{11} mode.

In order to simulate core-core mode conversion, a counter-propagating continuous probe beam is launched from the other end of the few mode fiber with the same wavelength of the writing beam. It is simple to choose the same wavelength for probe beam because the phase matching condition is naturally satisfied.

Assume the probe beam is pure fundamental mode (LP_{01}), when it travels through the grating, mode conversion occurs from LP_{01} fundamental core mode to the LP_{11} core mode, as seen in Figure 3-4(a) and Figure 3-4(b). Corresponding LP_{01} and LP_{11} modal powers are shown in Figure 3-4(c). During the simulation, the mesh size is chosen to be $\Delta x = \Delta y = 1$ μm and $\Delta z = 5$ μm to make sure the numerical accuracy. It is seen that full conversion (power is totally transferred from one mode to another) is achieved after a propagation of 1.02cm. Further propagation will make the converted LP_{11} mode couple back into the LP_{01} mode.

From Equation (2.13) it is seen that the mode conversion efficiency is dependent on the detuning parameter $\Delta = 2\pi/\Lambda - (\beta_{co} - \beta_m)$ and the coupling coefficient $|C_{co-m}|$. When phase matching condition is satisfied $\Delta = 0$, Equation (2.13) is reduced to $T_{co-z} = \cos^2(|C_{co-m}|z)$. Therefore full conversion can be obtained with a conversion length (the length that needs to achieve maximum conversion) $L = \pi/2|C_{co-m}|$. Since the coupling coefficient, or sometimes we call grating strength, is proportional to the strength of the refractive index modulation as well as the field overlap between the two converted modes, lower input power of the writing beam will induce a longer conversion length.

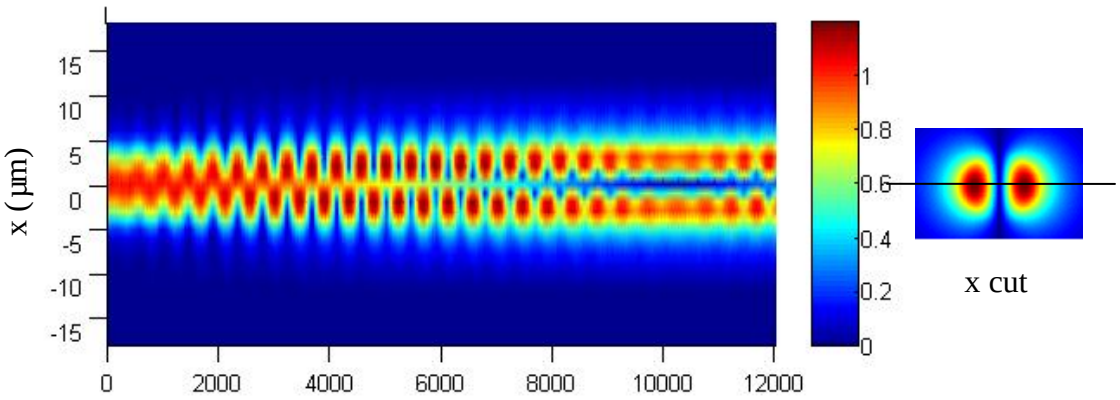

(a)

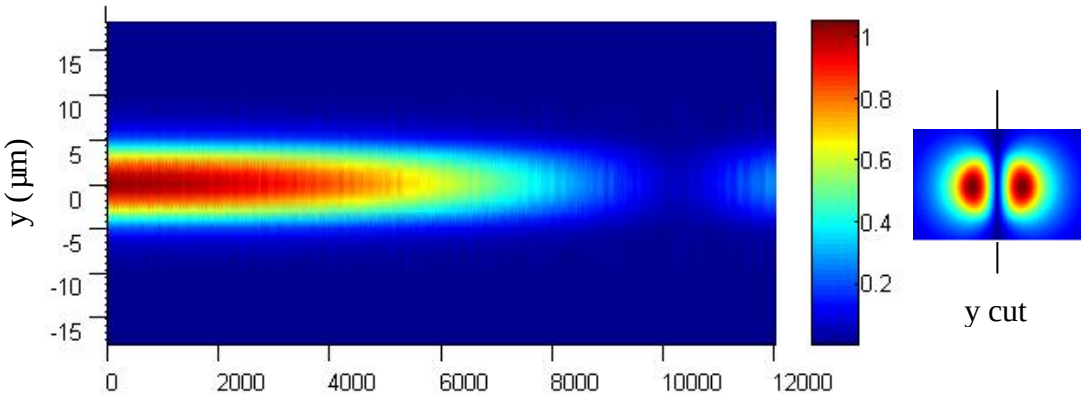

(b)

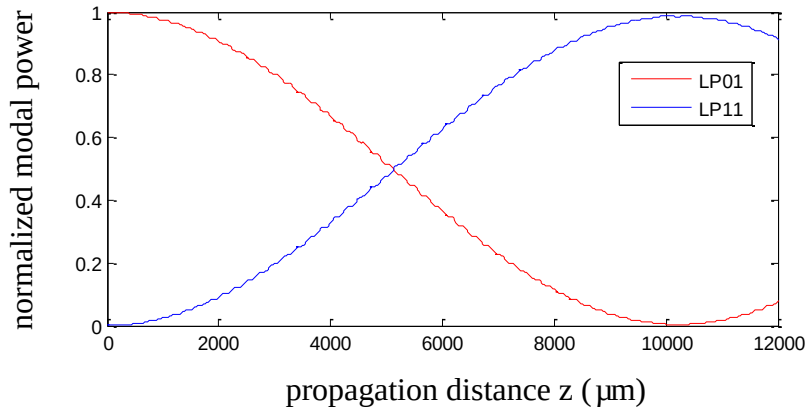

(c)

Figure 3-4 Mode evolution profile in the x-z plane (a) and y-z plane (b) when a LP_{01} mode is traveling through an OLPG. (c) corresponding normalized modal powers.

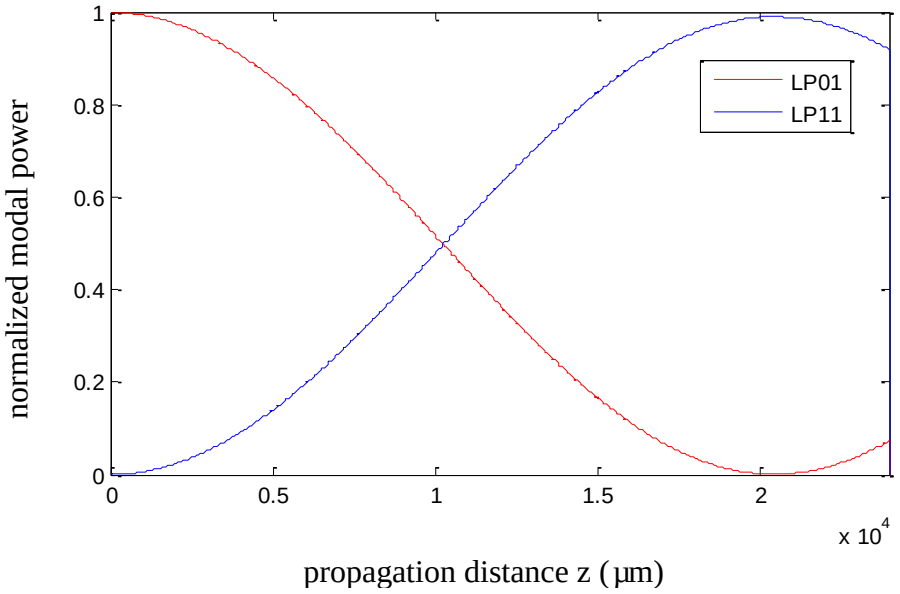

Figure 3-5 Normalized modal power as a function of propagation distance z. The total input power is 100 kW with 50% of the power in LP_{01} mode as well as in LP_{11} mode.

Figure 3-5 gives the normalized modal powers when the total input power is reduced to 100 kW while maintaining the same 50% power distribution for the two modes. Full conversion can be still achieved, as expected. However, the conversion length is 2.04 cm compared to the 1.02 cm for 200 kW of input power. The two times relationship agrees well with the theory since the coupling coefficient is doubled as the refractive index modulation is doubled when the input power is increased from 100 to 200 kW. From Equation (2.5), the coupling coefficient is also dependent on the profile of the refractive index modulation and therefore the power distribution of the two beating modes. If 25% of the input power is in LP_{01} mode, simulation results show a larger conversion length of 1.17 cm. If the grating length is only 1.02 cm which is the optimized length for the full conversion in the situation of 50% power in LP_{01} mode, the conversion efficiency for 25% of LP_{01} mode will reduce to 93%. After the calculation of the coupling coefficients for different power fraction of LP_{01} mode it is seen that 50% of LP_{01} will give the maximum coupling coefficient, as shown in Figure 3-6. At two boundaries 0% and 100%, there is no refractive index modulation and the coupling coefficients are zero.

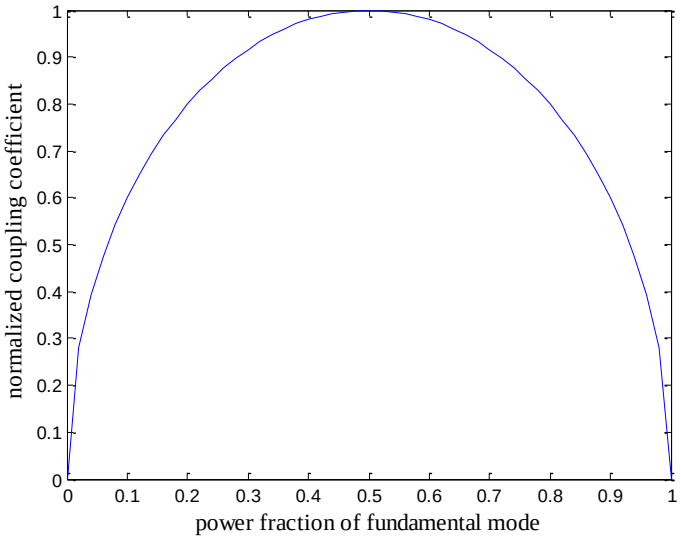

Figure 3-6 Normalized coupling coefficients for LP_{01} - LP_{11} core mode conversion as a function of power fractions of the LP_{01} core mode in the writing beam.

3.2.3 Simulation of core-cladding mode conversion

The optically induced LPG can also couple a core mode into a cladding mode if the phase matching condition is satisfied. Before using BPM to simulate the core-cladding mode coupling, it is necessary to calculate the phase matched wavelength which needs the effective indices of the core and cladding modes. The calculation of the refractive index for the fundamental core mode is obtained from [56]

$$V\sqrt{1-b}\,\frac{J_1(V\sqrt{1-b})}{J_0(V\sqrt{1-b})} = V\sqrt{b}\,\frac{K_1(V\sqrt{b})}{K_0(V\sqrt{b})}. \tag{3.52}$$

where J is the first kind Bessel function, K is the modified second Bessel function. $V = k_0 r_1 \sqrt{n_1^2 - n_2^2}$ is the normalized frequency and $b = (n_{eff}^2 - n_2^2)(n_1^2 - n_2^2)$ is the normalized propagation constant. r_1 is the core radius and n_1, n_2 are the refractive indices of the core and cladding, respectively. Equation (3.52) is usually called the characteristic equation for core guided modes in a fiber waveguide.

In order to calculate the effective index of the cladding mode, a third layer that is adjacent to the cladding needs to be considered. Conventionally the third layer is assumed

to be air if we do not consider ambient medium. A complex characteristic equation for the 3-layer structure was firstly derived by Erdogan [56] as

$$\frac{1}{\sigma_2}\frac{u_2\left(J\cdot K+\frac{\sigma_1\sigma_2 u_{21}u_{32}}{n_2^2 a_1 a_2}\right)\cdot p_m(a_2)-K\cdot q_m(a_2)+J\cdot r_m(a_2)-\frac{1}{u_2}s_m(a_2)}{-u_2\cdot\left(\frac{u_{32}}{a_2}J-\frac{u_{21}}{n_1^2 a_1}K\right)\cdot p_m(a_2)+\frac{u_{32}}{n_1^2 a_2}q_m(a_2)+\frac{u_{21}}{n_1^2 a_1}r_m(a_2)}$$
$$=\sigma_1\frac{u_2\left(\frac{u_{32}}{a_2}J-\frac{n_3^2 u_{21}}{n_2^2 a_1}K\right)\cdot p_m(a_2)-\frac{u_{32}}{a_2}\cdot q_m(a_2)-\frac{u_{21}}{a_1}\cdot r_m(a_2)}{u_2\cdot\left(\frac{n_3^2}{n_2^2}J\cdot K+\frac{\sigma_1\sigma_2 u_{21}u_{32}}{n_1^2 a_1 a_2}\right)\cdot p_m(a_2)-\frac{n_3^2}{n_1^2}K\cdot q_m(a_2)+J\cdot r_m(a_2)-\frac{n_2^2}{n_1^2 u_2}s_m(a_2)}. \tag{3.53}$$

where the inside parameters are defined as

$$\sigma_1=\frac{im}{\eta_0}n_{eff-clad},\sigma_1=im\eta_0 n_{eff-clad}, \tag{3.54}$$

$$u_{21}=\frac{1}{u_2^2}-\frac{1}{u_1^2},u_{32}=\frac{1}{w_3^2}-\frac{1}{u_2^2}, \tag{3.55}$$

$$u_1=k_0\sqrt{n_1^2-n_{eff-clad}^2},u_2=k_0\sqrt{n_2^2-n_{eff-clad}^2},w_3=k_0\sqrt{n_{eff-clad}^2-n_3^2}, \tag{3.56}$$

$$J=\frac{J_m'(u_1a_1)}{u_1J_m(u_1a_1)},K=\frac{K_m'(w_3a_2)}{w_3K_m(w_3a_2)}, \tag{3.57}$$

$$\begin{aligned}
p_m(r)&=J_m(u_2r)Y_m(u_2a_1)-J_m(u_2a_1)Y_m(u_2r),\\
q_m(r)&=J_m(u_2r)Y_m'(u_2a_1)-J_m'(u_2a_1)Y_m(u_2r),\\
r_m(r)&=J_m'(u_2r)Y_m(u_2a_1)-J_m(u_2a_1)Y_m'(u_2r),\\
s_m(r)&=J_m'(u_2r)Y_m'(u_2a_1)-J_m'(u_2a_1)Y_m'(u_2r).
\end{aligned} \tag{3.58}$$

Here a_1,a_2 are the radii of the core and cladding, respectively. $n_{eff-clad}$ is the effective index of the cladding mode. Thus, the effective index of the cladding mode can be calculated by solving Equation (3.53).

Although the effective index of the cladding mode can be obtained, mode fields as well as the differentiation between HE and EH modes are not shown from Equation (3.53). However, this can be solved by applying a transfer matrix method.

For a cylindrical step-index fiber structure, the longitudinal electric and magnetic fields have the general expressions

$$E_z = \left[AJ_\nu(ur) + BY_\nu(ur)\right]\exp(i\nu\varphi),$$
$$H_z = \left[CJ_\nu(ur) + DY_\nu(ur)\right]\exp(i\nu\varphi). \tag{3.59}$$

where $u = \sqrt{k_0^2\varepsilon - \beta^2}$ is the transverse wavevector. Assume the structure has 3 layers and each layer is denoted by i (i = 1, 2, 3) from core to the last layer, with boundaries located at r_1 and r_2. A transfer matrix is generated between adjacent layers through boundary conditions, i.e. continuity of the tangential E and H components. In the first layer, $B_1 = D_1 = 0$ and

$$E_z = A_1 J_\nu(u_1 r)\exp(i\nu\varphi),$$
$$H_z = C_1 J_\nu(u_1 r)\exp(i\nu\varphi). \tag{3.60}$$

Transverse components can be found in terms of E_z and H_z with

$$E_r = \frac{i}{\omega^2\varepsilon\mu - \beta^2}\left(\beta\frac{\partial E_z}{\partial r} + \frac{\mu\omega}{r}\frac{\partial H_z}{\partial\varphi}\right), \tag{3.61}$$

$$E_\varphi = \frac{i}{\omega^2\varepsilon\mu - \beta^2}\left(\frac{\beta}{r}\frac{\partial E_z}{\partial\varphi} - \mu\omega\frac{\partial H_z}{\partial r}\right), \tag{3.62}$$

$$H_r = \frac{i}{\omega^2\varepsilon\mu - \beta^2}\left(\beta\frac{\partial H_z}{\partial r} - \frac{\omega\varepsilon}{r}\frac{\partial E_z}{\partial\varphi}\right), \tag{3.63}$$

$$H_\varphi = \frac{i}{\omega^2\varepsilon\mu - \beta^2}\left(\frac{\beta}{r}\frac{\partial H_z}{\partial\varphi} + \omega\varepsilon\frac{\partial E_z}{\partial r}\right). \tag{3.64}$$

Thus, the tangential components in the first layer are

$$\begin{aligned}
E_z &= A_1 J_\nu(u_1 r)\exp(i\nu\varphi),\\
H_z &= C_1 J_\nu(u_1 r)\exp(i\nu\varphi),\\
E_\varphi &= \frac{i}{u_1^2}\left(\frac{i\beta\nu}{r}A_1 J_\nu(u_1 r) - \mu_1\omega u_1 C_1 J_\nu'(u_1 r)\right)\exp(i\nu\varphi),\\
H_\varphi &= \frac{i}{u_1^2}\left(\frac{i\beta\nu}{r}C_1 J_\nu(u_1 r) + \omega\varepsilon_1 u_1 A_1 J_\nu'(u_1 r)\right)\exp(i\nu\varphi).
\end{aligned} \tag{3.65}$$

Rewrite it with a matrix form

$$\begin{bmatrix} E_z \\ H_z \\ E_\varphi \\ H_\varphi \end{bmatrix} = M_1 \begin{bmatrix} A_1 \\ 0 \\ C_1 \\ 0 \end{bmatrix} = e^{iv\varphi} \begin{bmatrix} J_\nu(u_1 r) & 0 & 0 & 0 \\ 0 & 0 & J_\nu(u_1 r) & 0 \\ -\dfrac{\beta\nu}{u_1^2 r} J_\nu(u_1 r) & 0 & -\dfrac{i\mu_1\omega}{u_1} J_\nu'(u_1 r) & 0 \\ \dfrac{i\omega\varepsilon_1}{u_1} J_\nu'(u_1 r) & 0 & -\dfrac{\beta\nu}{u_1^2 r} J_\nu(u_1 r) & 0 \end{bmatrix} \begin{bmatrix} A_1 \\ 0 \\ C_1 \\ 0 \end{bmatrix}. \tag{3.66}$$

It is the same for the fields in the second layer

$$\begin{bmatrix} E_z \\ H_z \\ E_\varphi \\ H_\varphi \end{bmatrix} = M_2 \begin{bmatrix} A_2 \\ B_2 \\ C_2 \\ D_2 \end{bmatrix}$$

$$= e^{iv\varphi} \begin{bmatrix} J_\nu(u_2 r) & Y_\nu(u_2 r) & 0 & 0 \\ 0 & 0 & J_\nu(u_2 r) & Y_\nu(u_2 r) \\ -\dfrac{\beta\nu}{u_2^2 r} J_\nu(u_2 r) & -\dfrac{\beta\nu}{u_2^2 r} Y_\nu(u_2 r) & -\dfrac{i\mu_2\omega}{u_2} J_\nu'(u_2 r) & -\dfrac{i\mu_2\omega}{u_2} Y_\nu'(u_2 r) \\ \dfrac{i\omega\varepsilon_2}{u_2} J_\nu'(u_2 r) & \dfrac{i\omega\varepsilon_2}{u_2} Y_\nu'(u_2 r) & -\dfrac{\beta\nu}{u_2^2 r} J_\nu(u_2 r) & -\dfrac{\beta\nu}{u_2^2 r} Y_\nu(u_2 r) \end{bmatrix} \begin{bmatrix} A_2 \\ B_2 \\ C_2 \\ D_2 \end{bmatrix}. \tag{3.67}$$

The fields in the last layer are simplified to

$$\begin{bmatrix} E_z \\ H_z \\ E_\varphi \\ H_\varphi \end{bmatrix} = M_3 \begin{bmatrix} A_3 \\ 0 \\ C_3 \\ 0 \end{bmatrix} = e^{iv\varphi} \begin{bmatrix} K_\nu(w_3 r) & 0 & 0 & 0 \\ 0 & 0 & K_\nu(w_3 r) & 0 \\ \dfrac{\beta\nu}{w_3^2 r} K_\nu(w_3 r) & 0 & \dfrac{i\mu_3\omega}{w_3} K_\nu'(w_3 r) & 0 \\ -\dfrac{i\omega\varepsilon_3}{w_3} K_\nu'(w_3 r) & 0 & \dfrac{\beta\nu}{w_3^2 r} K_\nu(w_3 r) & 0 \end{bmatrix} \begin{bmatrix} A_3 \\ 0 \\ C_3 \\ 0 \end{bmatrix}. \tag{3.68}$$

with $w_3 = \sqrt{\beta^2 - k_0^2 \varepsilon_3}$.

Applying the boundary conditions yields

$$\begin{aligned} &M_1(r_1)\begin{bmatrix} A_1 & 0 & C_1 & 0 \end{bmatrix}^T = M_2(r_1)\begin{bmatrix} A_2 & B_2 & C_2 & D_2 \end{bmatrix}^T, \\ &M_2(r_2)\begin{bmatrix} A_2 & B_2 & C_2 & D_2 \end{bmatrix}^T = M_3(r_2)\begin{bmatrix} A_3 & 0 & C_3 & 0 \end{bmatrix}^T. \end{aligned} \tag{3.69}$$

that is,

$$\begin{aligned} &M_1(r_1)\begin{bmatrix} A_1 & 0 & C_1 & 0 \end{bmatrix}^T = M\begin{bmatrix} A_3 & 0 & C_3 & 0 \end{bmatrix}^T, \\ &M = M_2(r_1)M_2(r_2)^{-1}M_3(r_2). \end{aligned} \tag{3.70}$$

Rewrite Equation (3.70) to

$$N\begin{bmatrix} A_1 & C_1 & A_3 & C_3 \end{bmatrix}^T = 0,$$
$$N = \begin{bmatrix} M_1(1,1) & M_1(1,3) & -M(1,1) & -M(1,3) \\ M_1(2,1) & M_1(2,3) & -M(2,1) & -M(2,3) \\ M_1(3,1) & M_1(3,3) & -M(3,1) & -M(3,3) \\ M_1(4,1) & M_1(4,3) & -M(4,1) & -M(4,3) \end{bmatrix}. \tag{3.71}$$

Nonzero solution of Equation (3.71) requires

$$\det N = 0. \tag{3.72}$$

For a fixed azimuthal number ν, Equation (3.72) has a set of solutions β with two types of modes HE and EH. At $\nu = 0$, odd solutions correspond to TE modes and even solutions correspond to TM modes. For $\nu \geq 1$, odd solutions represent HE modes and even solutions represent EH modes [57]. Moreover, the coefficients in each layer can be derived after solving β, therefore the mode fields are obtained. It is noticed that we still use $HE_{\nu m}$ or $EH_{\nu m}$ to define the cladding mode. Although we also define a core mode in the same way, the difference is the cladding modes are numbered from the first cladding mode with the effective index lower and closest to the cladding index (for the structure with $n_1 > n_2 > n_3$), while the core modes are numbered from the first core modes with the effective index lower and closest to the core index.

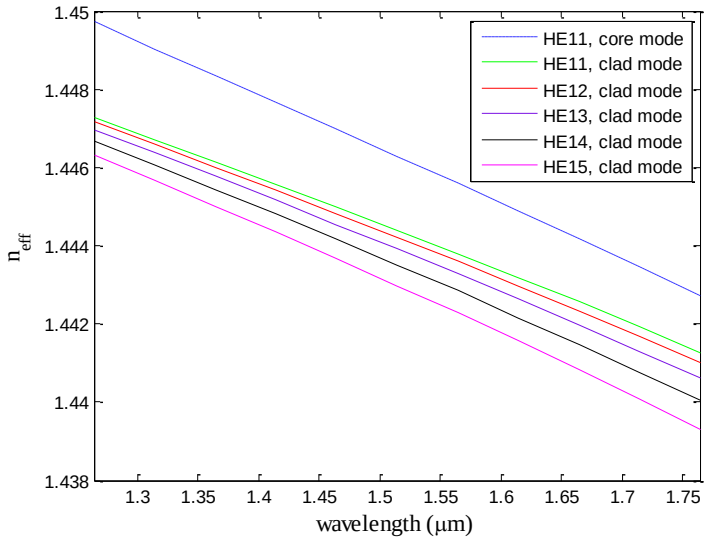

(a)

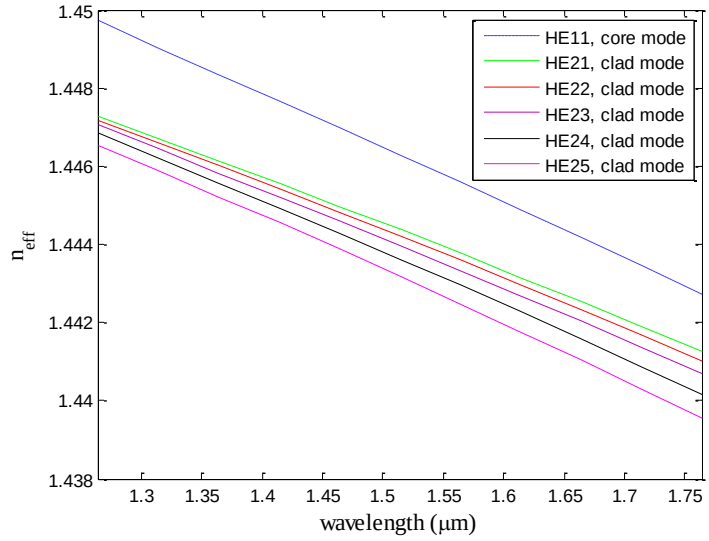

(b)

Figure 3-7 Effective refractive indices of some cladding modes (a) HE_{11} - HE_{15} and (b) HE_{21} - HE_{25} in a Corning SMF28. The effective index of the fundamental core mode is also given as a reference.

Figure 3-7 shows the calculated effective indices of some cladding modes in a Corning SMF28. Like the existence of linearly polarized core modes in an optical fiber, linearly polarized cladding modes also exist as a constitution of some cladding modes with nearly the same effective index. A $LP_{v,m}$ cladding mode is the combination of $HE_{v+1,m}$ and $EH_{v-1,m}$ cladding modes.

Given the effective index, phase matched wavelength (resonant wavelength) for a certain cladding mode can be calculated from Equation (2.14). In addition to the phase matching condition, coupling coefficient is another important factor that determines the full conversion length at the phase matched wavelength. A smaller coupling coefficient increases the conversion length, and mode conversion will not occur if the coupling coefficient is zero. For a refractive index perturbation profile with no azimuthal dependence, HE_{11} core mode can be only transferred to the cladding mode with the same azimuthal number $\nu = 1$. However, the index perturbation profile in OLPG is asymmetric with a $\cos\varphi$ dependence since it is generated by the beating of LP_{01} symmetric and LP_{11} asymmetric mode. The possible converted cladding mode are asymmetric LP_{1m} modes.

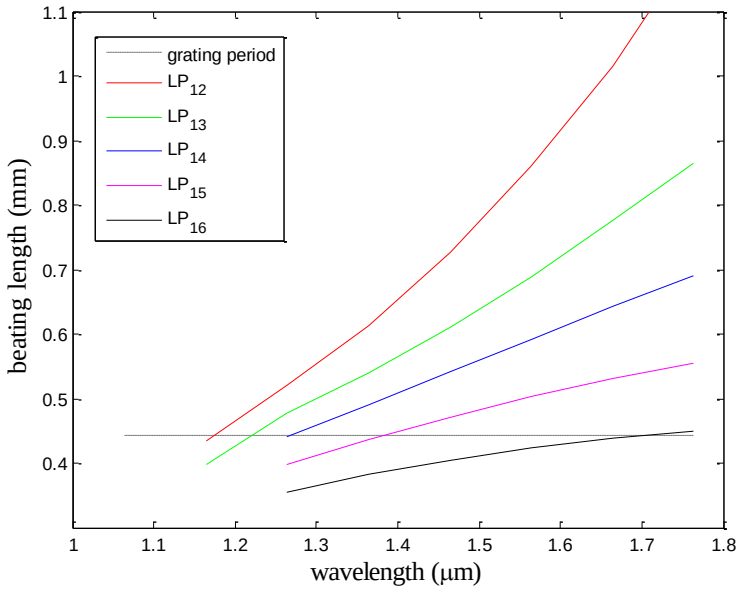

Figure 3-8 Beating lengths ($2\pi / \Delta\beta$) between LP_{01} core mode and LP_{1m} (m = 2,..., 6) cladding modes. The OLPG grating period (444 μm) is given as a reference.

Figure 3-8 shows the beating lengths $2\pi / \Delta\beta$ between LP_{01} core mode and LP_{1m} (m = 2, ..., 6) cladding modes. The dashed line represents the grating period formed by the beating of LP_{01} and LP_{11} core modes at 1064 nm. It shows that the resonant wavelengths for LP_{1m} (m = 2, ..., 6) cladding modes are 1.1778, 1.2100, 1.2714, 1.3867 and 1.705 μm, respectively. At these wavelengths, LP_{01} core mode can be transferred to LP_{1m} cladding modes. This can be further verified by the BPM result shown in Figure 3-9.

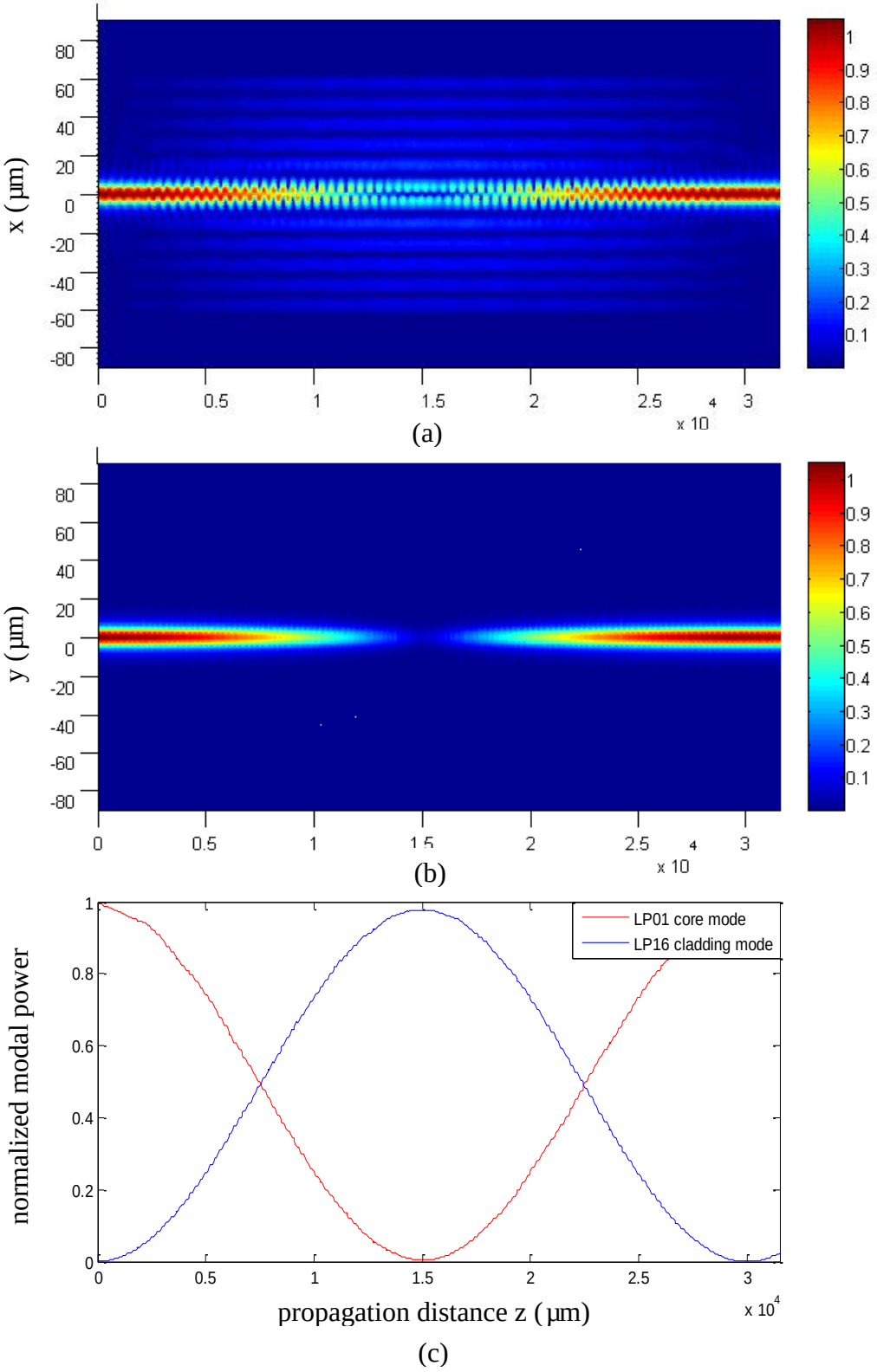

Figure 3-9 Conversion between LP_{01} core mode and LP_{16} cladding mode at 1.705 μm. (a) Mode evolution in x-z plane, (b) mode evolution in y-z plane and (c) modal powers.

From Figure 3-9 it is seen that after traveling 1.5 cm full conversion occurs between LP_{01} fundamental core mode and LP_{16} cladding mode right at the phase matched wavelength 1.705 μm, as predicted. Here we assume the fiber is still Corning SMF28. The grating is created by a writing beam with a total power of 800 kW and 50% of the power in LP_{01} mode as well as in the LP_{11} mode. Such a high power is chosen to simplify the simulation since the conversion length is reduced and therefore the simulation steps. As previously stated, the full conversion length at the phase matched wavelength is inversely proportional to the coupling coefficient, and therefore the power of writing beam. Figure 3-10 illustrates that the full conversion length is doubled from 1.5 cm to 3.0 cm when the power of writing beam is reduced from 800 kW to 400 kW. Moreover, if a launched writing power is in the order of kilowatts, the length required to achieve full conversion could go up to the order of meters.

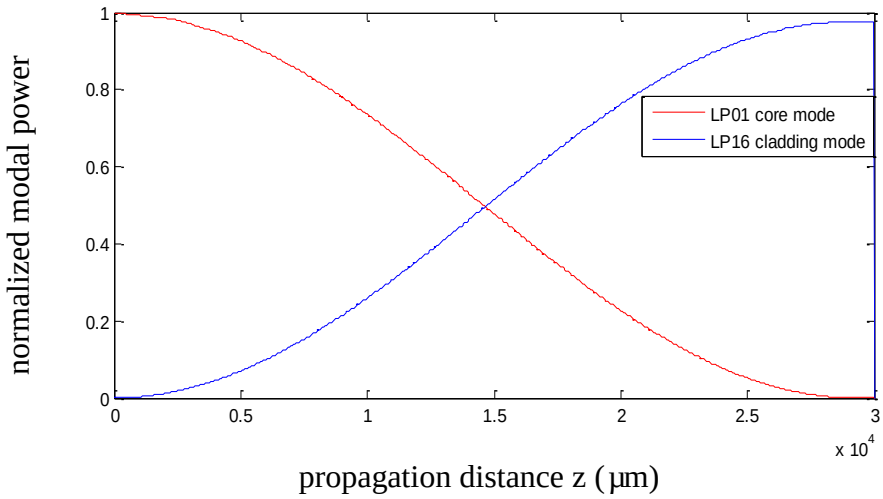

Figure 3-10 Conversion between LP_{01} core mode and LP_{16} cladding mode at 1.705 μm with a total writing power of 400 kW and 50% of the power in LP_{01} mode as well as in LP_{11} mode.

Full conversion behavior is also observed for LP_{15} cladding mode at the phase matched wavelength of 1.3867 μm with a conversion length of 2.08 cm. Corresponding normalized modal power is given in Figure 3-11.

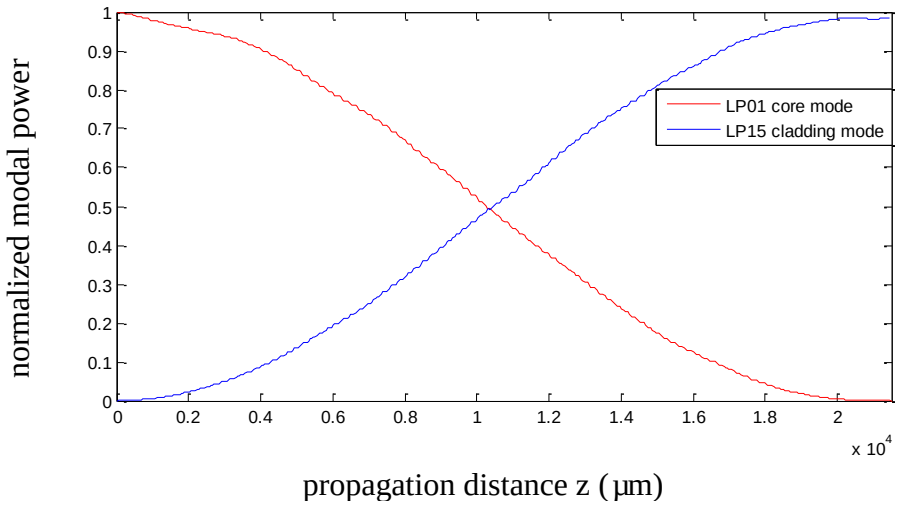

Figure 3-11 Conversion between LP_{01} core mode and LP_{15} cladding mode at 1.3867 μm with a total writing power of 400 kW and 50% of the power in LP_{01} mode as well as in LP_{11} mode.

Mode coupling theory tells us that conversion efficiency will not achieve unity under phase mismatched condition $\Delta \neq 0$. Larger detuning will result in lower conversion efficiency. Figure 3-13 shows the conversion when scanning the wavelength around 1.705 μm. The fiber is SMF28 with a writing power of 400 kW which is evenly distributed on the LP_{01} and LP_{11} core modes. It is seen that the FWHM for the resonant band is around 63 nm. From Equation (2.13) we can calculate the conversion efficiency

$$\eta(z) = \frac{1}{1+\left(\frac{\Delta}{2}/\left|C_{co-m}(z)\right|\right)^2}. \tag{3.73}$$

It is shown that for a 50% conversion efficiency, large coupling coefficient will induce a broader Δ_{FWHM} and therefore a broader bandwidth $\Delta\lambda_{FWHM}$. For a writing power of 800 kW, the FWHM can go up to 127 nm. The relation between the FWHM and the writing beam power is shown in Figure 3-12 with a nearly linear dependence and a slope of 0.16 nm/kW. When the writing power is only 10 kW, the FWHM can be as low as 1.6 nm.

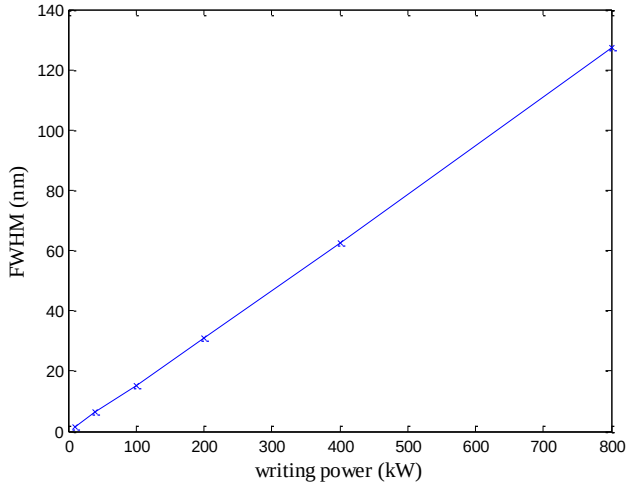

Figure 3-12 FWHM of the conversion efficiency for the resonant band at 1.3867 μm as a function of writing power.

Although full conversion cannot be obtained for phase mismatch, the conversion length will be shortened as given by

$$L_c = \frac{\pi}{2\sqrt{|C_{co-m}|^2 + (\frac{\Delta}{2})^2}}. \tag{3.74}$$

From Equation (3.74) we can see that for a fixed coupling coefficient the conversion length becomes smaller as the detuning parameter is larger.

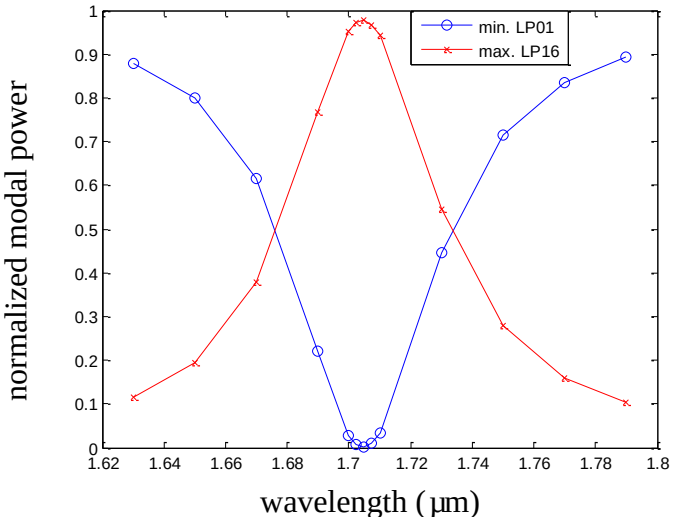

Figure 3-13 Conversion behavior with a detuning of wavelength. Phase matched wavelength is 1.705 μm.

If we enlarge the spectral range, other resonant bands which correspond to the coupling to other cladding modes can also be observed. Figure 3-14 demonstrates the converted LP_{01} modal power as a function of probe wavelength from 1.2 μm to 1.9 μm at the writing power of 400 kW and is evenly distributed to LP_{01} and LP_{11} core modes. Material dispersion is included in the simulation with the Sellmeier coefficients for SMF28. It is clearly seen that several separate resonant bands are located at 1.2100 μm, 1.2714 μm, 1.3867 μm and 1.7050 μm, which correspond to the coupling between core LP_{01} mode to LP_{13}, LP_{14}, LP_{15} and LP_{16} cladding modes, respectively. It needs to be noticed that Figure 3-14 is not the transmission spectrum. It only represents the minimum normalized power of LP_{01} mode, with a value of unity if no conversion occurs and zero if full conversion occurs.

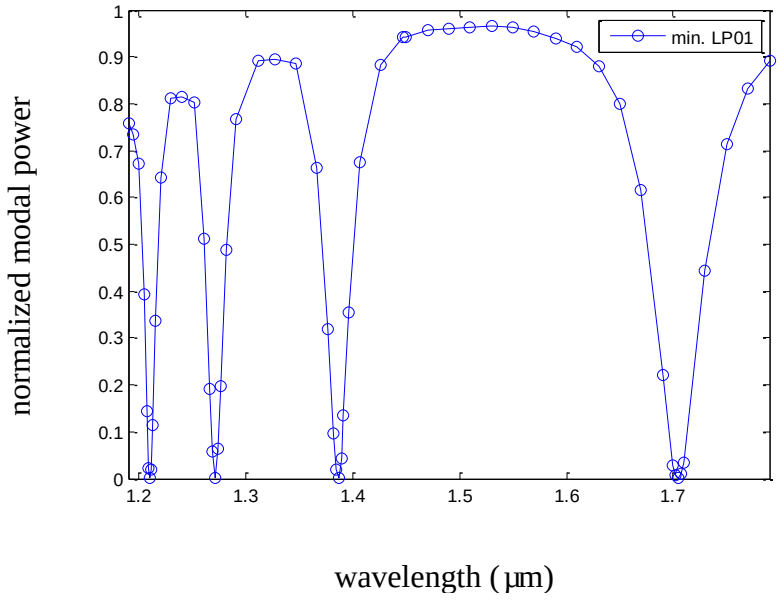

Figure 3-14 Minimum normalized power of LP_{01} core mode as a function of probe wavelength. Resonant bands correspond to LP_{13}, LP_{14}, LP_{15} and LP_{16} cladding modes, respectively.

3.3 Temperature sensors

The sensing mechanism can be explained based on the phase matching condition (Equation (2.14)), which can be rewritten as

$$\lambda = \Lambda(n_{co}^{eff} - n_{cl,m}^{eff}) = \Delta n_{eff}\Lambda. \tag{3.75}$$

where Λ is the OLPG grating period, Δn_{eff} is the effective index difference between the core and cladding modes at probe wavelength λ. Unlike traditional LPGs with a fixed, inscribed gratings, the grating of OLPG depends on the effective index difference between two core modes at the writing wavelength with a period of

$$\Lambda = 2\pi / \left| \beta_{lm}^{write} - \beta_{l'm'}^{write} \right|. \tag{3.76}$$

where β_{lm}^{write} and $\beta_{l'm'}^{write}$ denote the propagation constants for (l, m) and (l', m') core modes at writing wavelength. The temperature sensitivity is

$$\frac{d\lambda}{dT} = \frac{d\lambda}{d\Delta n_{eff}} \frac{d\Delta n_{eff}}{dT} + \frac{d\lambda}{d\Lambda} \frac{d\Lambda}{dT}. \tag{3.77}$$

The wavelength shift is a function of the change in the differential effective index with temperature $d\Delta n_{eff} / dT$ as well as the change in the grating period. Compared to a traditional LPG, the change of grating period in OLPG is not due to thermal expansion but due to the variation of effective index difference at writing wavelength. This variation may be very subtle compared to the variation induced by thermal expansion in a traditional LPG.

In the simulation, it is required to know the thermo-optic coefficients of the core dn_{co} / dT and cladding dn_{cl} / dT. For the Corning SMF28, the cladding is fabricated with pure silica and the core is Ge-doped silica. According to [38], we approximate the thermo-optic coefficient of cladding $dn_{cl} / dT = 7.8 \times 10^{-6} / ℃$. The thermo-optic coefficient of the core is $dn_{co} / dT = 7.97 \times 10^{-6} / ℃$ which is slightly higher due to the doping process. Based on the thermo-optic coefficients, the resonant band shift as a function of temperature is demonstrated in Figure 3-15(a) with a range of 400 ℃ and a reference of 30 ℃. The fiber in the simulation is SMF28 with the OLPG generated by

LP_{01} and LP_{11} core modes with equal power at 1064 nm. The temperature-induced variation of the OLPG grating period Λ is also taken into consideration. Moreover, it is assumed that the ambient refractive index is $n_3 = 1$.

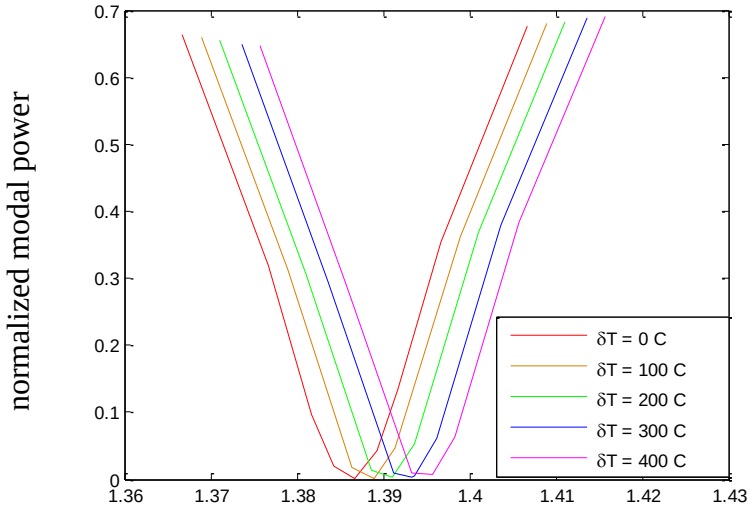

(a)

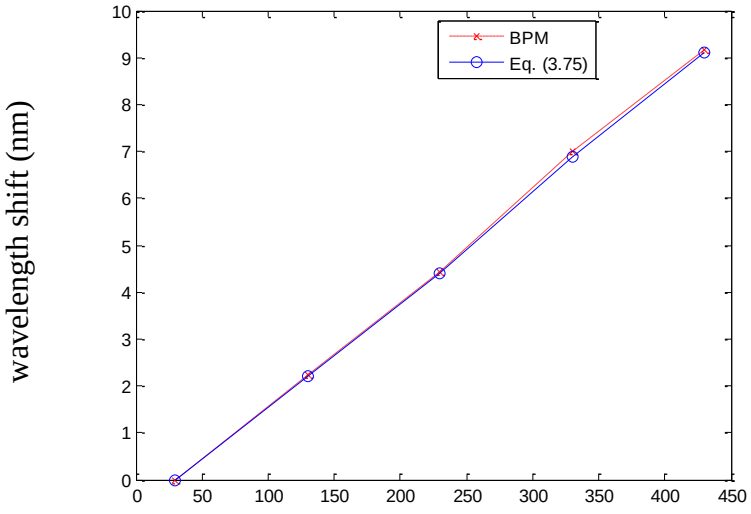

(b)

Figure 3-15 (a) Resonant band shift at temperatures ΔT = 0°C, 100°C, 200°C, 300°C and 400 ℃. (b) Corresponding wavelength shift as a function of temperature.

The selected resonant band corresponds to the coupling of LP_{01} core mode to LP_{15} cladding mode at 1.3867 μm. The calculated wavelength shift is given in Figure 3-15(b) with a sensitivity of 2.3 nm/100 ℃ after a curve fitting. It is seen from Figure 3-15(b) that the wavelength shift has a nearly linear response of temperature. The band shift depicted in Figure 3-15(a) is calculated by BPM with the corresponding wavelength shift plotted in Figure 3-15(b) (red dash). As a comparison, resonant wavelength calculated from the phase matching condition (Equation (3.75)) is plotted in Figure 3-15(b) (blue solid). It is shown that the predicted wavelength by BPM agrees well with the phase matching condition.

Figure 3-16 depicts the calculated wavelength shift for different resonant bands as a function of temperature. The bands are located at 1.3867 μm (A), 1.2714 μm (B) and 1.2100 μm (C), respectively. Corresponding slope rates are 2.28 nm/100 ℃, 2.21 nm/100 ℃ and 2.14 nm/100 ℃. It is seen from Figure 3-16 that three modes have slightly different sensitivities which are due to the distinct changes in Δn_{eff} . If we compare to the result given by a traditional LPG inscribed in a SMF28 with a period of 280 μm [38], the sensitivity of OLPG can achieve the same order of magnitude as a traditional LPG.

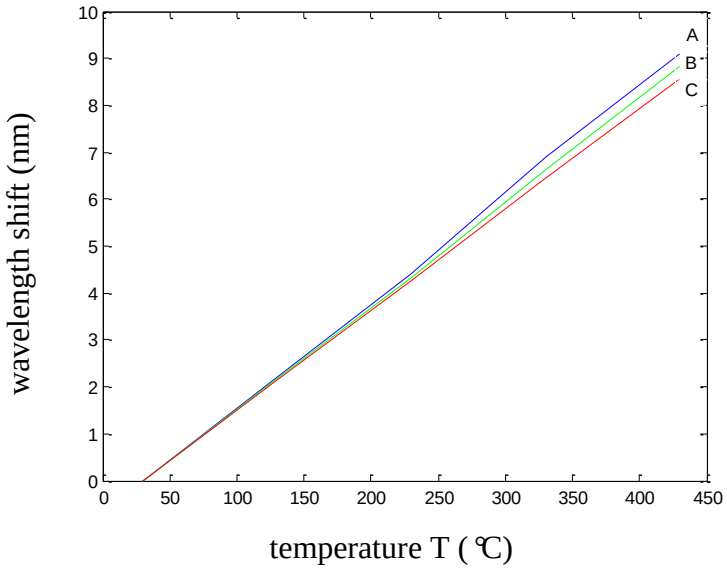

Figure 3-16 Temperature-induced wavelength shift for different bands located at 1.3867 μm (A), 1.2714 μm (B) and 1.2100 μm (C).

3.4 Axial strain sensors

Like the temperature sensitivity, the strain sensitivity has a form of

$$\frac{d\lambda}{d\varepsilon} = \frac{d\lambda}{d\Delta n_{eff}} \frac{d\Delta n_{eff}}{d\varepsilon} + \frac{d\lambda}{d\Lambda} \frac{d\Lambda}{d\varepsilon}. \tag{3.78}$$

The difference of OLPG from a traditional LPG is also the second term with the grating period Λ only depending on the effective index difference of the two core modes at the writing wavelength. There is no mechanical strain-induced extension of the grating period in OLPG.

Like the simulation of temperature sensitivity, the simulation of strain sensitivity requires the elasto-optic coefficients for the core and cladding. Axial strain will affect the core and cladding indices as well as their diameters. Assume the fiber is a homogeneous material in elasticity (the Young's modulus and Poisson's ratio are considered to be the same for both core and cladding). The variation of core and cladding diameter due to Poisson's effect has the following expression [58]

$$\frac{dr}{d\varepsilon} = -\nu r. \tag{3.79}$$

where $r = r_1, r_2$ are the core and cladding radii, ν is the Poisson's ratio with a value of 0.17 for cladding (fused silica) and 0.165 for core (3% Ge-doped fused silica). The strain-induced refractive index perturbation is [58]

$$\frac{dn}{d\varepsilon} = -\frac{n^3}{2}\left[p_{12} - (p_{11} + p_{12})\nu\right]. \tag{3.80}$$

where $n = n_1, n_2$ are the core and cladding refractive indices, p_{11}, p_{12} are the strain-optic coefficients with values of $p_{11} = 0.12$ and $p_{12} = 0.27$ [58].

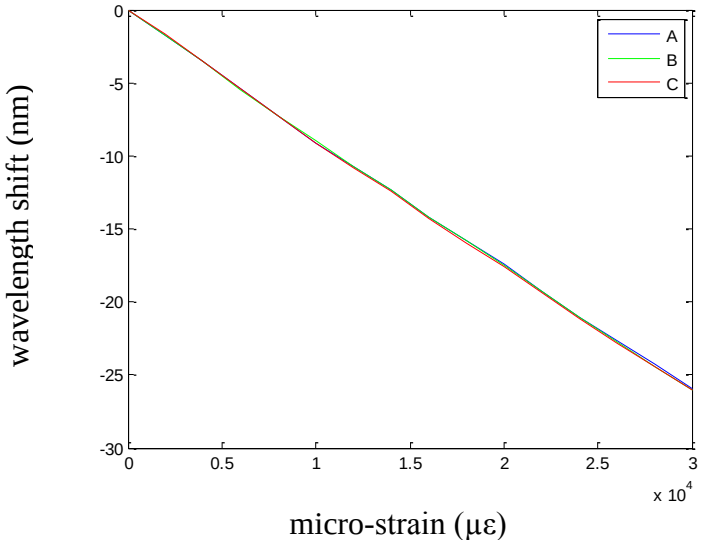

Figure 3-17 Wavelength shift for different bands as a function of strain.

Figure 3-17 depicts the calculated wavelength shift for the different resonant bands (1.3867 μm (A), 1.2714 μm (B) and 1.2100 μm (C)) as a function of axial strain με. The fiber is the same SMF28 with an ambient refractive index is $n_3 = 1$. The variation of the OLPG grating period Λ is also taken into consideration. After a linear curve fitting it is seen that the three bands have very close sensitivity with a value of -8.8 nm/%ε.

Figure 3-18 shows the calculated strain-induced wavelength shift for the 1.3867 μm band at different ambient indices n_3 = 1.0, 1.33 and 1.44. The sensitivity undergoes a slight decrease from n_3 = 1.0 to n_3 = 1.33 with a value from -8.72 nm/%ε to -8.96 nm/%ε, and a further large decrease for n_3 = 1.44 with a value of -14.24 nm/%ε. The dependence of the strain sensitivity on ambient index shows a similar trend compared to the traditional LPG [38].

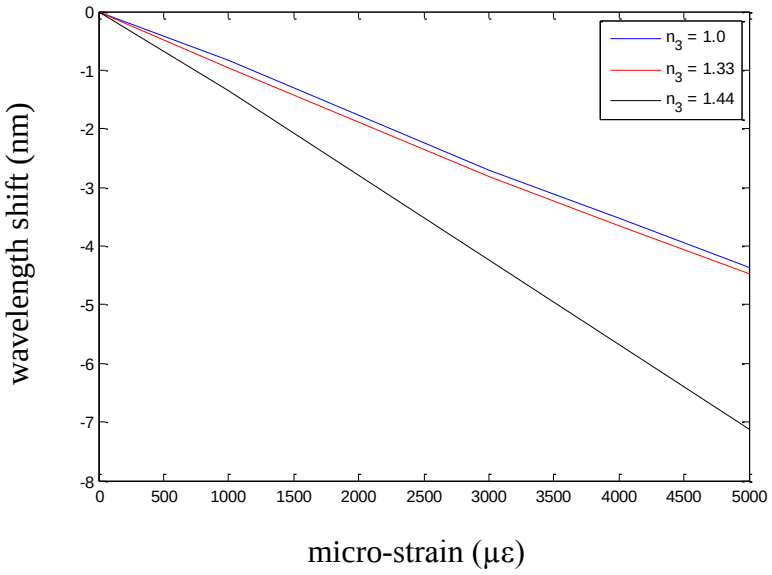

Figure 3-18 Wavelength shift as a function of strain for the band at 1.38 μm under different ambient indices n_3 = 1.0 (blue), 1.33 (red) and 1.44 (black).

3.5 Refractive index (RI) sensors

As the effective indices of the cladding modes depend on the ambient index, OLPG can be used for RI sensing. As a RI sensor, it is assumed that the effective indices of the guided core modes (LP_{01} and LP_{11}) are not influenced by the ambient index if the cladding radius is very large (like $r_2 = 62.5\mu m$ in SMF28). Therefore the grating period Λ remains unchanged $d\Lambda / dn_3 = 0$. The sensitivity is then given by

$$\frac{d\lambda}{dn_3} = \frac{d\lambda}{d\Delta n_{eff}} \frac{d\Delta n_{eff}}{dn_3} = \frac{d\lambda}{dn_{cl}^{eff}} \frac{dn_{cl}^{eff}}{dn_3}. \tag{3.81}$$

From Equation (3.81) it is seen that OLPG should behave like an LPG for RI sensing when the cladding radius is very large such that Λ is wavelength-independent.

Figure 3-19 demonstrates the calculated wavelength shift for the three different resonant bands located at 1.3867 μm (A), 1.2714 μm (B) and 1.2100 μm (C) as a function of ambient index from 1.0 to 1.44. The shift refers to the wavelength at n_3 = 1.0. The fiber is SMF28 with the OLPG generated by the LP_{01} and LP_{11} core modes at 1064 nm. It is seen

that the magnitude of the wavelength shift increases with the order of resonant band (from C to A), which can be explained by Equation (2.22). Moreover, for a single resonant band the shift varies gradually when n_3 changes from 1.0 to 1.3. When n_3 is closer to the cladding index, the shift varies more rapidly. This behavior, which is similar to the traditional LPG [38], is due to the large effective index variation of the cladding mode as the ambient index approaches the cladding index. The shifts for bands A, B and C from ambient index n_3 = 1.0 to n_3 = 1.44 are -17.8 nm, -5.7 nm and -2.0 nm, respectively. When the ambient index is further increased over the cladding mode index, the cladding mode becomes lossy with a complex propagation constant. So in the simulation we only consider the ambient index lower than the cladding index to make sure cladding mode is still guided.

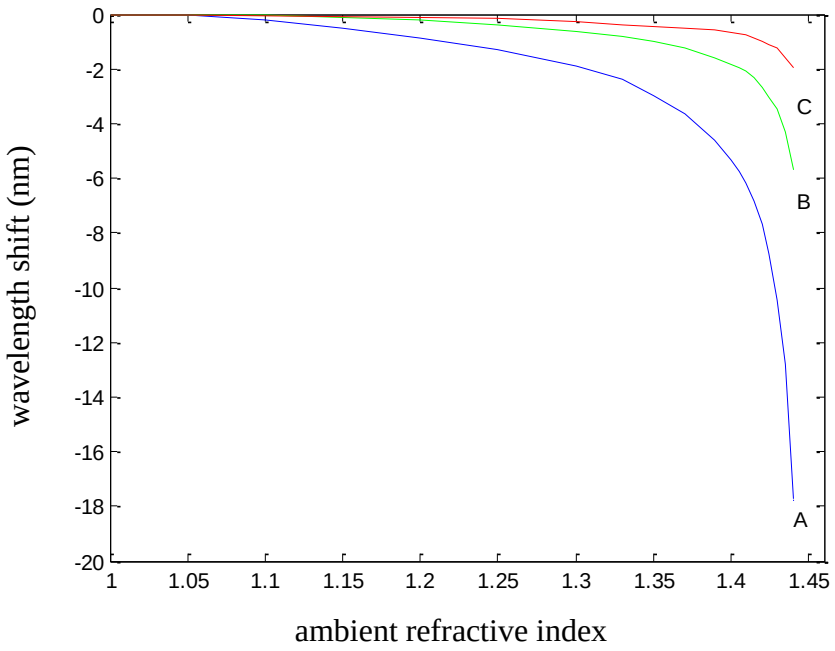

Figure 3-19 Theoretically predicted wavelength shift for different resonant bands as a function of ambient refractive index from 1.0 to 1.44. The resonant bands are located at 1.3867 μm (A), 1.2714 μm (B) and 1.2100 μm (C).

3.6 System of OLPG-based distributed fiber sensors

A simple system of OLPG-based distributed fiber sensors is shown in Figure 3-20. A high power pulsed laser (usually 1064 nm Nd: YAG laser) is coupled into a few mode fiber (SMF28 can be used as a dual mode fiber when operating at 1064 nm). Careful alignment is needed to make sure both LP_{01} and LP_{11} core modes are excited and share the same power. Therefore a transient and traveling OLPG is formed through the two modes interference with the period equal to the beating length. The half-wave plate and polarizer placed right after the pulsed laser are used to control the power of the writing beam. The output of the writing beam is imaged and captured by a beam profiler to observe the two modes interference.

On the other hand, a counter-propagating continuous-wave probe beam is coupled into the few mode fiber. Careful alignment is also needed to make sure only LP_{01} core mode is excited. The source of the probe beam is a tunable laser with the tuning range covering at least one of the resonant bands shown in Figure 3-14. The transmitted probe beam is captured and coupled into a single mode fiber (SMF) after reflected by a non-polarizing beam splitter (NPBS) which is used to prevent the detection of polarization changes. The received transmitted probe beam is then detected and analyzed by the photodiode receiver and oscilloscope. Two long pass filters are used in the system with one placed before the tunable laser to filter the strong transmitted writing beam and protect the tunable laser, and the other placed before the receiver to filter the strong reflected writing beam. The two long pass filters are designed to pass the tunable laser and prevent the 1064 nm high pulsed laser. The sensing scheme is to scan the probe beam within a spectral range and record the time-domain signal of the transmitted probe beam for each wavelength. When plotting the transmitted signal as a function of the probe wavelength and time, time-domain signal indicates the sensing points within the fiber while spectral-domain shows the resonant bands for every sensing point. Therefore it is possible to use OLPG as a distributed fiber sensor.

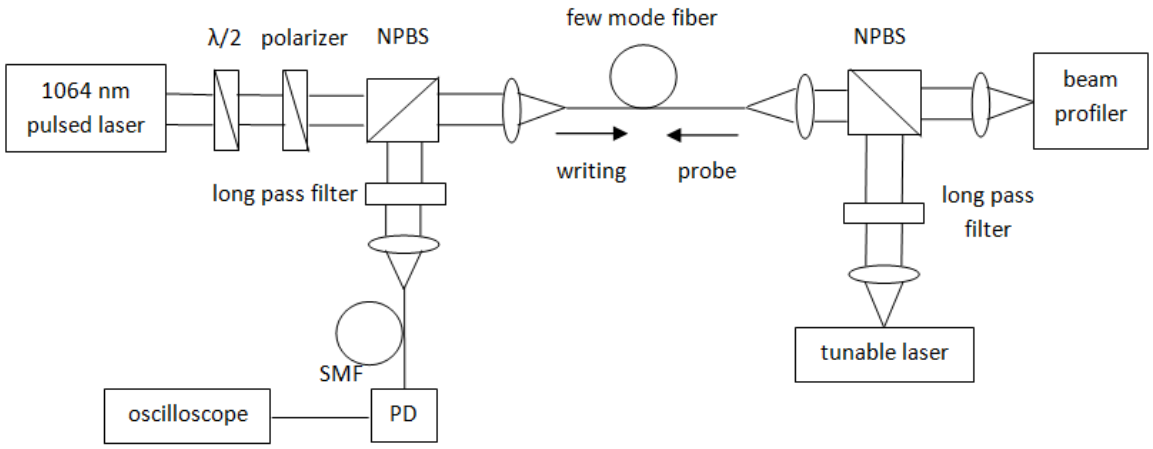

Figure 3-20 System of the OLPG-based fiber sensor. NPBS: non-polarizing beam splitter, λ/2: half-wave plate, SMF: single mode fiber, PD: photodiode receiver.

3.7 Analysis of the OLPG-based fiber sensors

Although simulation result shows OLPG can be used for mode conversion and fiber sensing with a basic system shown in Figure 3-20. The sensing system has some limitations and drawbacks, one of which is the complexity and high cost. At first, two optical sources are required in the system - high power pulsed laser and a tunable laser which greatly increase the system cost. Secondly, the system needs free-space to fiber coupling for both the writing and the probe beams, and careful alignment is needed to control the excited modes. It is hard to implement an all-fiber based system due to the high writing power. Furthermore, there is a high selectivity of the tunable laser source which needs to cover the resonant bands. The simulation result shows several resonant bands locating at 1.705 μm, 1.3867 μm, 1.271 μm and 1.2100 μm. Usually a commonly used C-band tunable laser only covers from 1520-1570 nm. Then it is unable to observe the mode conversion using a C-band tunable laser. However, it is possible to manipulate the resonant bands by choosing other few mode fibers or changing the fiber cladding diameter. The previous option requires special fibers which may be costly. The later one can be achieved through etching the fiber cladding on a common SMF28.

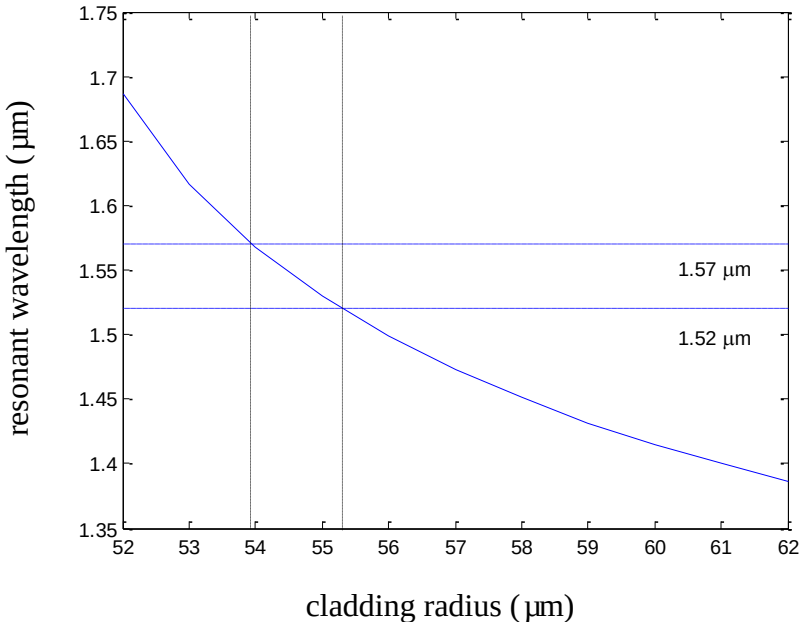

Figure 3-21 Resonant wavelength as a function of the cladding radius. The resonant band corresponds to the LP_{15} cladding mode.

Figure 3-21 depicts the resonant wavelength as a function of the cladding radius for the LP_{15} cladding mode. It is seen that the resonant wavelength moves to longer wavelength when the cladding radius is reduced. This behavior is the same compared to the result in [59] and can be simply explained as the effective index of the cladding mode is decreased when the cladding radius becomes smaller. Moreover, we can see that in order to move the resonant wavelength into the tunable laser spectral range (1520-1570 nm), the cladding radius needs to be located within 54 μm and 55.3 μm.

Previous simulation is based on the situation that the power of LP_{01} and LP_{11} core modes are evenly distributed. The choice of that is due to the largest coupling coefficient when the writing power is evenly distributed. Different power distributions will reduce the coupling coefficient and therefore increase the conversion length. Figure 3-6 already shows that for the core-core mode coupling, 50% power of LP_{01} as well as LP_{11} writing modes will maximize the coupling coefficient. Here the normalized coupling coefficient of LP_{01} core mode to LP_{15} cladding mode is also calculated and given in Figure 3-22 from which we can see that optimal power distribution is 50% of LP_{01} as well as LP_{11}.

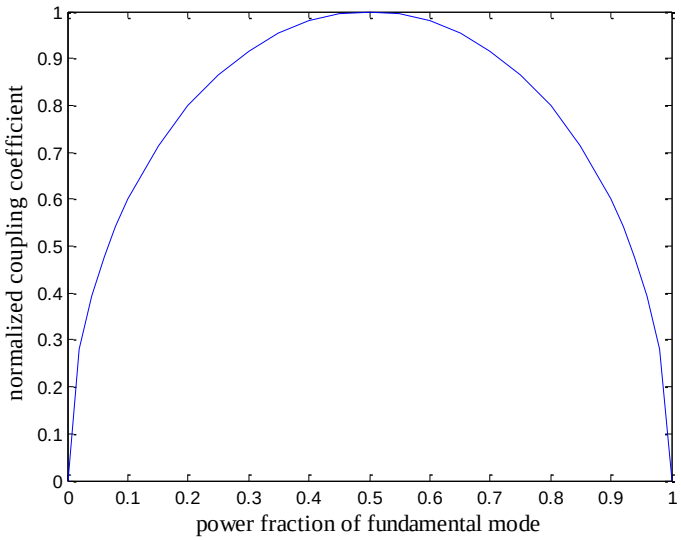

Figure 3-22 Normalized coupling coefficient for LP_{01} core mode to LP_{15} cladding mode coupling as a function of the power fractions of the LP_{01} core mode in the writing beam.

The alignment for the power distribution of LP_{01} and LP_{11} core modes is significant since the coupling coefficient varies from different power distributions. A small power distribution of LP_{01} or LP_{11} mode will reduce the coupling coefficient, and at two boundaries of 0% LP_{01} and 100% LP_{01} the coupling coefficient reduces to zero and no mode conversion will occur. However, good news is that the coupling coefficient does not drop too much when the power fraction of LP_{01} core mode is within 25% to 75%. It is seen from Figure 3-22 that the coupling coefficient can still maintain 86.6% when the power fraction of LP_{01} core mode is 25% or 75%. The 86.6% efficiency will elongate the conversion length to 1/86.6% = 1.154 times. Figure 3-23 shows a full conversion length of 2.4 cm that is exactly 1.154 times of the conversion length of 2.08 cm (see Figure 3-11) for 50% power of LP_{01} mode.

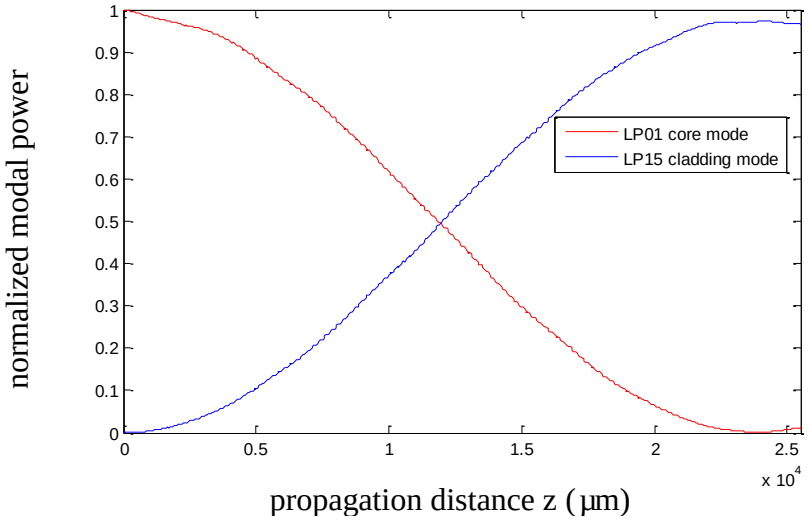

Figure 3-23 Conversion between LP_{01} core mode and LP_{15} cladding mode at 1.3867 μm with a total writing power of 400 kW and 25% of the power in LP_{01} mode.

Although we know how to shift the resonant wavelength into C-band and understand the effect of the writing mode power distribution, it is important to understand another factor - how much input writing power is needed such that we can observe evident mode conversion. Previous simulation uses an input power of 400 kW which is very large and ideal except using femtosecond lasers. Now suppose we use a 1064 nm Q-switched laser with a duration of 10 ns which corresponds to the grating length of ~ 2 m. Here assume the light speed in few mode fiber is 2×10^8 m/s and neglect the pulse shape. When the input writing power is only 1 kW with a 50% of the power in LP_{01}, the corresponding conversion length for LP_{15} cladding mode will be as large as ~ 8.32 m which is greater than the grating length. The transmission after traveling through a 2 m OLPG will be as high as 86.4%, and this value will be higher if considering the pulse shape. When the input power is 4.04 kW with corresponding conversion length right at 2 m, the transmission will be zero after traveling through the OLPG. In fact, zero transmission is ideal and cannot be obtained if we consider the pulse shape and modal loss. If the power is further increased with a corresponding conversion length smaller than the pulse width, the converted cladding mode will couple back into the core mode and therefore increase the transmission. However, if we consider the attenuation of the cladding mode, the converted cladding mode will not fully couple back into the LP_{01} core mode. Another

important factor is the FWHM of the resonant band, as discussed in Section 3.2.3. A low writing power will induce a very narrow FWHM which makes the resonant bands difficult to be observed. Simulation result shows that for a 4 kW writing power the FWHM for the band at 1.3867 μm is as narrow as 0.2 nm. Such a narrow band needs you to scan the tunable laser in a very fine step in order to find the resonant bands.

Chapter 4 Conclusions

In this thesis we have proposed to use an optically induced long-period grating for distributed sensing. Compared to the gratings formed by acoustic wave, optically induced gratings can travel for a longer distance due to the small attenuation of guided core modes. The motivation of using OLPG for distributed sensing originates from the distributed measurement of ambient index which cannot be achieved by other mature techniques such as Brillouin scattering or Raman scattering mechanisms.

Before accessing OLPG, traditional LPGs are discussed at first in Chapter 2. Several main techniques for LPG fabrication are introduced like the inscription by UV light, residual thermal stress, mechanical stress and etching. Then the coupled mode theory is given to theoretically explain the mode conversion in an LPG. The properties and applications of LPG sensors are further discussed.

After a review of traditional LPGs, OLPG is proposed in Chapter 3 with an introduction of the basic principle and numerical analysis showing the full mode conversion in OLPG when phase matching condition is satisfied. After demonstrating the core-cladding mode conversion in OLPG, the application of OLPG as a sensor is analyzed. Temperature, axial strain and refractive index sensitivities are calculated and compared to traditional LPGs. It is shown that for temperature and axial strain sensing, the variation of grating period in OLPG is due to the variation of the effective index difference at writing wavelength while for a traditional LPG it is directly affected by temperature through thermal expansion or mechanical strain through strain-induced physical elongation. The system for OLPG-based distributed fiber sensors is also proposed along with some analysis including the drawbacks and limitations of the system, moving of the resonant wavelength into C-band and the effect of the writing power as well as the power distribution.

Future efforts are needed in the area, of which the most important is the experimental demonstration of the distributed sensing. The experiment is challenging since the whole system involves the coupling from free-space to fiber, the excitation of LP_{01} and LP_{11}

modes for the writing beam and the excitation of only LP_{01} core mode for the probe beam. Both excitations need very careful alignments. Moreover, the resonant band is not located within the C-band where common tunable lasers are readily available. An appropriate solution is given by etching the cladding radius and move the resonant wavelengths.

References

1. Vengsarkar, A.M. Long period fiber gratings. in Optical Fiber Communications, 1996. OFC '96. 1996.
2. Singh, A., et al., Temperature sensitivity of long period fiber grating in SMF-28 fiber. Optik - International Journal for Light and Electron Optics, 2014. **125**(1): p. 457-460.
3. Chunn-Yenn, L., L.A. Wang, and G.-W. Chern, Corrugated long-period fiber gratings as strain, torsion, and bending sensors. Lightwave Technology, Journal of, 2001. **19**(8): p. 1159-1168.
4. Patrick, H.J., et al., Hybrid fiber Bragg grating/long period fiber grating sensor for strain/temperature discrimination. Photonics Technology Letters, IEEE, 1996. **8**(9): p. 1223-1225.
5. Yi-Ping, W., J. Wei, and D.N. Wang, Strain Characteristics of CO_2-Laser-Carved Long Period Fiber Gratings. Quantum Electronics, IEEE Journal of, 2007. **43**(2): p. 101-108.
6. Schuster, T., et al., Miniaturized Long-Period Fiber Grating Assisted Surface Plasmon Resonance Sensor. Lightwave Technology, Journal of, 2012. **30**(8): p. 1003-1008.
7. Wang, D.Y., et al., Fully Distributed Fiber-Optic Hydrogen Sensing Using Acoustically Induced Long-Period Grating. Photonics Technology Letters, IEEE, 2011. **23**(11): p. 733-735.
8. Posey, R., Jr., G.A. Johnson, and S.T. Vohra, Strain sensing based on coherent Rayleigh scattering in an optical fibre. Electronics Letters, 2000. **36**(20): p. 1688-1689.
9. Dakin, J.P., et al., Distributed optical fibre Raman temperature sensor using a semiconductor light source and detector. Electronics Letters, 1985. **21**(13): p. 569-570.
10. Kurashima, T., T. Horiguchi, and M. Tateda, Distributed-temperature sensing using stimulated Brillouin scattering in optical silica fibers. Optics Letters, 1990. **15**(18): p. 1038-1040.
11. Bao, X., et al., Experimental and theoretical studies on a distributed temperature sensor based on Brillouin scattering. Lightwave Technology, Journal of, 1995. **13**(7): p. 1340-1348.
12. Hotate, K. and M. Tanaka, Distributed fiber Brillouin strain sensing with 1-cm spatial resolution by correlation-based continuous-wave technique. Photonics Technology Letters, IEEE, 2002. **14**(2): p. 179-181.
13. Kreger, S.T., et al. High-resolution extended distance distributed fiber-optic sensing using rayleigh backscatter. 2007.
14. Kung, A., et al., Rayleigh fiber optics gyroscope. Photonics Technology Letters, IEEE, 1997. **9**(7): p. 973-975.
15. Arya, V., et al., Microbend losses in singlemode optical fibers: theoretical and experimental investigation. Lightwave Technology, Journal of, 1995. **13**(10): p. 1998-2002.

16. Andermahr, N. and C. Fallnich, Optically induced long-period fiber gratings for guided mode conversion in few-mode fibers. Optics Express, 2010. **18**(5): p. 4411-4416.
17. Vengsarkar, A.M., et al., Long-period fiber gratings as band-rejection filters. Lightwave Technology, Journal of, 1996. **14**(1): p. 58-65.
18. Rao, Y.J., et al., Novel long-period fiber gratings written by high-frequency CO_2 laser pulses and applications in optical fiber communication. Optics Communications, 2004. **229**(1–6): p. 209-221.
19. Hwang, I.K., S.H. Yun, and B.Y. Kim, Long-period fiber gratings based on periodic microbends. Optics Letters, 1999. **24**(18): p. 1263-1265.
20. Hill, K.O., et al., Efficient mode conversion in telecommunication fibre using externally written gratings. Electronics Letters, 1990. **26**(16): p. 1270-1272.
21. Dianov, E.M., et al., Refractive-index gratings written by near-ultraviolet radiation. Optics Letters, 1997. **22**(4): p. 221-223.
22. Duhem, O. and M. Douay, Effect of UV-induced birefringence on long-period-grating coupling characteristics. Electronics Letters, 2000. **36**(5): p. 416-417.
23. Martinez-Rios, A., et al., Long period fibre gratings. Fiber Optic Sensors, M. Yasin, ed.
24. Davis, D.D., et al. CO_2 laser-induced long-period fibre gratings: spectral characteristics, cladding modes and polarisation independence. Electronics Letters, 1998. **34**, 1416-1417.
25. Kondo, Y., et al., Fabrication of long-period fiber gratings by focused irradiation of infrared femtosecond laser pulses. Optics Letters, 1999. **24**(10): p. 646-648.
26. Rego, G., et al., High-temperature stability of long-period fiber gratings produced using an electric arc. Lightwave Technology, Journal of, 2001. **19**(10): p. 1574-1579.
27. Davis, D.D., et al. Long-period fibre grating fabrication with focused CO_2 laser pulses. Electronics Letters, 1998. **34**, 302-303.
28. Dianov, E.M., et al. Long-period fiber gratings and mode-field converters fabricated by thermodiffusion in phosphosilicate fibers. in Optical Communication, 1998. 24th European Conference on. 1998.
29. Dianov, E.M., et al. Thermo-induced long-period fibre gratings. in Integrated Optics and Optical Fibre Communications, 11th International Conference on, and 23rd European Conference on Optical Communications (Conf. Publ. No.: 448). 1997.
30. Kakarantzas, G., et al., Miniature all-fiber devices based on CO_2 laser microstructuring of tapered fibers. Optics Letters, 2001. **26**(15): p. 1137-1139.
31. Humbert, G. and A. Malki, Electric-arc-induced gratings in non-hydrogenated fibres: fabrication and high-temperature characterizations. Journal of Optics A: Pure and Applied Optics, 2002. **4**(2): p. 194.
32. Spillman, W.B., Multimode fiber-optic pressure sensor based on the photoelastic effect. Optics Letters, 1982. **7**(8): p. 388-390.
33. Chunn-Yenn, L., G.-W. Chern, and L.A. Wang, Periodical corrugated structure for forming sampled fiber Bragg grating and long-period fiber grating with tunable coupling strength. Lightwave Technology, Journal of, 2001. **19**(8): p. 1212-1220.

34. Yariv, A., Coupled-mode theory for guided-wave optics. Quantum Electronics, IEEE Journal of, 1973. **9**(9): p. 919-933.
35. Grattan, K.T. and B. Meggitt, Optical fiber sensor technology. Vol. 1. 1995: Springer.
36. Xuewen, S., Z. Lin, and I. Bennion, Sensitivity characteristics of long-period fiber gratings. Lightwave Technology, Journal of, 2002. **20**(2): p. 255-266.
37. Stephen, W.J., et al., Cryogenic temperature response of fibre optic long period gratings. Measurement Science and Technology, 2003. **14**(8): p. 1409.
38. Bhatia, V., Properties and sensing applications of long-period gratings. 1996.
39. Liu, Y., L. Zhang, and I. Bennion, Fibre optic load sensors with high transverse strain sensitivity based on long-period gratings in B/Ge co-doped fibre. Electronics Letters, 1999. **35**(8): p. 661-663.
40. Martinez-Rios, A., D. Monzon-Hernandez, and I. Torres-Gomez, Highly sensitive cladding-etched arc-induced long-period fiber gratings for refractive index sensing. Optics Communications, 2010. **283**(6): p. 958-962.
41. Khaliq, S., S.W. James, and R.P. Tatam, Enhanced sensitivity fibre optic long period grating temperature sensor. Measurement Science and Technology, 2002. **13**(5): p. 792.
42. Xu, M.G., et al., Independent tuning of cascaded long period fibre gratings for spectral shaping. Electronics Letters, 1997. **33**(22): p. 1893-1894.
43. Liu, Y., J.A.R. Williams, and I. Bennion, Optical bend sensor based on measurement of resonance mode splitting of long-period fiber grating. Photonics Technology Letters, IEEE, 2000. **12**(5): p. 531-533.
44. Jacob, et al. Effects of Fiber Core Concentricity Error and UV Illumination Direction on the Bend Direction Asymmetry of Long-Period Gratings. in Bragg Gratings, Photosensitivity, and Poling in Glass Waveguides. 1999. Stuart, Florida: Optical Society of America.
45. Ye, C.C., S.W. James, and R.P. Tatam, Simultaneous temperature and bend sensing with long-period fiber gratings. Optics Letters, 2000. **25**(14): p. 1007-1009.
46. Feit, M.D. and J.A. Fleck, Computation of mode eigenfunctions in graded-index optical fibers by the propagating beam method. Applied Optics, 1980. **19**(13): p. 2240-2246.
47. Feit, M.D. and J.A. Fleck, Computation of mode properties in optical fiber waveguides by a propagating beam method. Applied Optics, 1980. **19**(7): p. 1154-1164.
48. Yevick, D. and L. Thylén, Analysis of gratings by the beam-propagation method. Journal of the Optical Society of America, 1982. **72**(8): p. 1084-1089.
49. Neyer, A., et al., A beam propagation method analysis of active and passive waveguide crossings. Lightwave Technology, Journal of, 1985. **3**(3): p. 635-642.
50. Kaczmarski, P., P. Lagasse, and J. Vandewege, Propagating-beam model for a single-mode-fibre fused coupler. Optoelectronics, IEE Proceedings J, 1987. **134**(2): p. 111-116.
51. Xu, C. and W. Huang, Finite-difference beam propagation method for guide-wave optics. Progress In Electromagnetics Research, 1995. **11**: p. 1-49.

52. Hadley, G.R., Transparent boundary condition for the beam propagation method. Quantum Electronics, IEEE Journal of, 1992. **28**(1): p. 363-370.
53. Berenger, J.-P., A perfectly matched layer for the absorption of electromagnetic waves. Journal of Computational Physics, 1994. **114**(2): p. 185-200.
54. Tsuji, Y. and M. Koshiba, Finite element beam propagation method with perfectly matched layer boundary conditions for three-dimensional optical waveguides. International Journal of Numerical Modelling: Electronic Networks, Devices and Fields, 2000. **13**(2-3): p. 115-126.
55. Tsuji, Y. and M. Koshiba, Finite element beam propagation method with perfectly matched layer boundary conditions for three-dimensional optical waveguides. International Journal of Numerical Modelling: Electronic Networks, Devices and Fields, 2000. **13**(2-3): p. 115-126.
56. Erdogan, T., Cladding-mode resonances in short- and long-period fiber grating filters. Journal of the Optical Society of America A, 1997. **14**(8): p. 1760-1773.
57. Oleg, V.I., A.N. Sergei, and V.G. Yurii, Cladding modes of optical fibers: properties and applications. Physics-Uspekhi, 2006. **49**(2): p. 167.
58. Huang, S.Y., J.N. Blake, and K. Byoung-Yoon, Perturbation effects on mode propagation in highly elliptical core two-mode fibers. Lightwave Technology, Journal of, 1990. **8**(1): p. 23-33.
59. McCall, M., On the application of coupled mode theory for modeling fiber Bragg gratings. Lightwave Technology, Journal of, 2000. **18**(2): p. 236-242.